

Article

Nature of Paleozoic Basement of the Catalan Coastal Ranges (Spain) and Tectonic Setting of the Priorat DOQ Wine Terroir: Evidence from Volcanic and Sedimentary Rocks

Pavel Kepezhinskas ^{1,*}, Nikolai Berdnikov ¹, Nikita Kepezhinskas ², Natalia Konovalova ¹, Valeria Krutikova ¹ and Ivan Astapov ¹

¹ Institute of Tectonics and Geophysics, Khabarovsk 680063, Russia

² APEX Geoscience, Edmonton, AB T5M 3Y7, Canada

* Correspondence: pavel_k7@yahoo.com

Abstract: The Paleozoic volcano-sedimentary rocks within the structural basement of the horst-and-graben system of the Catalan Coastal Ranges (CCR) are composed of black shale, volcanoclastic sediments, lava flows, sills and lithocrystalloclastic tuffs. Paleozoic sediments are depleted in high-field strength elements (HFSE) such as Nb, Ta, Zr, Hf and Ti, suggesting their accumulation within the Andean-type active continental margin environment. Volcanic rocks within the Paleozoic CCR sequence belong to shoshonitic and high-K volcanic series and are enriched in Cs, Rb and Ba and depleted in HFSE, which is consistent with their derivation from metasomatized (possibly through deep recycling of pelagic sediments) subduction-related mantle source. The presence of sills (sill-sediment complex) suggests that Paleozoic basement of the CCR was formed within the rifted active continental margin or an arc-back-arc basin system akin to the modern Western Pacific subduction configuration. This complex volcanic terroir hosts world-class wines of the Priorat DOQ region. The presence of framboidal pyrite and magnetite, siderite, sphalerite xenotime, (La–Ce–Nd)-monazite, zircon and baddeleyite, as well as cuprite, tenorite and cupriferous and native silver in volcanic-derived black shale (and consequently in the world-famous “llicorella” soil overlying it) may have had dramatic effects on wine quality and sensory characteristics. These mineral features, together with strong enrichment of Priorat shale in Au, Ag and, to a lesser extent, Pt could have pronounced effects on (1) rates and specific types of chemical reactions; (2) plant metabolism; (3) response to nutrient components and (4) determination of grape flavor. Volcanic wine terroirs, such as the Priorat DOQ region, are special geologic environments for wine growth, capable of producing unique wine aromatic and gustatory characteristics.

Keywords: Catalan Coastal Ranges; Priorat DOQ; Paleozoic basement; black shale; shoshonite; metasomatized mantle sources; rifted active continental margin; volcanic wine terroirs



Citation: Kepezhinskas, P.; Berdnikov, N.; Kepezhinskas, N.; Konovalova, N.; Krutikova, V.; Astapov, I. Nature of Paleozoic Basement of the Catalan Coastal Ranges (Spain) and Tectonic Setting of the Priorat DOQ Wine Terroir: Evidence from Volcanic and Sedimentary Rocks. *Geosciences* **2023**, *13*, 31. <https://doi.org/10.3390/geosciences13020031>

Academic Editors: Salvatore Critelli and Jesus Martinez-Frias

Received: 13 December 2022

Revised: 12 January 2023

Accepted: 24 January 2023

Published: 26 January 2023



Copyright: © 2023 by the authors. Licensee MDPI, Basel, Switzerland. This article is an open access article distributed under the terms and conditions of the Creative Commons Attribution (CC BY) license (<https://creativecommons.org/licenses/by/4.0/>).

1. Introduction

The concept of terroir in winemaking is a centuries-old idea primarily originated in the internationally renowned wine regions of Bordo and Burgundy [1–5]. The prominent enologist Jake Hancock defined terroir in a very simple and efficient way as “a delimited area with its own characteristic geology, climate and methods of viticulture” [3]. Similar, but to a lesser or greater degree of detail, formulations of the wine terroir definitions were introduced in Italy, Alsace, South Africa, Australia and Canada [6–11]. It also appears to be generally well understood among earth scientists and viticulturists alike that specific relationships between terroir characteristics and various qualities of wine are at the very least quite difficult to quantify [12,13]. Nevertheless, the tectonic setting of wine terroirs appears to play an important role in determining the general location, topography and geologic properties of individual vineyards, types of grapes that are grown within this or

that particular terroir or vineyard and ultimately in the aromatic and gustatory qualities of individual wines [3,5,9,10,14–18].

The concept of geochemical terroir fingerprinting is based on the supposition that the chemical elements as well as stable and radiogenic isotopes in the igneous, metamorphic and sedimentary rocks and overlying soils derived from them may be transferred to the grapevine and, ultimately, to the final product, e.g., wine [19–25]. For example, several studies suggest that the distribution of rare earth elements (REE) in the vineyard soil is also maintained in the grapevine tissues [26,27]. Similarly, major and trace element patterns in rocks and soils in various wine appellations in France, Italy, Spain, South Africa and Canada were shown to be reflected in the chemical compositions of bulk grapes as well as grape skin, seeds and flesh [14,20,21,23]. Other studies have suggested that the trace element compositions of grape berries may have variable effects on wine quality and its aromatic and gustatory characteristics [18,19,22].

Some of the most exciting and noteworthy wines grow in the vicinity of prominent Quaternary volcanoes (Vesuvius, Etna, Roccamonfina, Mount Hood, Lassen Peak, Monte Vulture) or are associated with ancient volcanic soils and terranes derived from the volcanoes of the distant geologic past [28–31]. These volcanic terroirs occur within different tectonic regimes, ranging from within-plate oceanic island volcanoes (Azores, Canary Islands) to leaky transform faults (Etna), continental flood basalt provinces (Columbia River, Walla Walla, Snake River Plain), continental grabens and rifts (Rhine and Mosel) and to modern volcanoes (Vesuvius, Lassen Peak, Ararat, Aragatz, Aeolian Islands, Santorini) and paleo-volcanic terranes (Willamette Valley, Napa, Andean volcanic belt) of Phanerozoic subduction zones [7,9,16,25,28,30,32,33]. We present in this paper new results on the mineralogy and geochemistry of Paleozoic black shale and associated volcanic rocks from the Priorat DOQ (Denominació d'Origen Qualificada) region in the Catalan Coastal Ranges (CCR) of NE Spain, with implications for the general nature of the CCR's Paleozoic basement and tectonic setting of volcanic wine terroirs.

2. Geologic Background and Samples

The Priorat DOQ region is located within the western flank of the Catalan Coastal Ranges (CCR), which extend over 250 km along the northeast coast of the Iberian Peninsula (Figure 1). The Paleozoic basement of the CCR is composed of a series of tectonic nappes separated by NE–SW-oriented listric faults and decollements [34,35] and are flanked by the Ebro structural basin (foreland basin of the Pyrenees) to the NW and by the Valencia Trough within the Mediterranean Sea shelf to the SE (Figure 1). The post-Paleozoic structure of the CCR is essentially a complex system of asymmetrical ENE–WSW to NE–SW-striking horsts and grabens with a general NW tilt [36,37]. Horsts (Pre-Littoral and Littoral systems in Figure 1) are composed of ~1.2 km-thick Carboniferous–Permian volcanic-sedimentary basement with discordant Mesozoic cover, while grabens (Pre-Littoral depression in Figure 1) are filled with almost 4 km of the Miocene to Recent continental molasse sediments [36,37]. The Cenozoic tectonic evolution of the CCR to a substantial extent inherits Mesozoic compressional structures and is largely controlled by complex interplay of compressional and extensional tectonics related to the Paleogene reactivation of the Montmell–Garraf extensional basin [38].

All samples used in this study were collected from natural outcrops and road cuts (Figure 2) along the highways connecting Gratallops, El Lloar, Torroja del Priorat, El Molar, La Vilella Baixa and La Cartuja De Escaladei. Paleozoic black shale (principal source of the famous “llicorella” wine soil), volcanoclastic mudstone and siltstone (biotite-rich shale) and tuffaceous sandstone form large (several tens to hundreds of meters) asymmetrical, overturned and recumbent folds and contain subordinate amounts of mostly aphyric to weakly plagioclase–porphyritic lava flows, basaltic sills and felsic to intermediate tuffaceous material (Figure 2A,B,E). Volcanic (lava and lithocrystalloclastic tuffs) layers typically range in thickness from several centimeters to 1–2 m (Figure 2C,D). The entire Paleozoic volcano-

sedimentary package in the Priorat region is pervasively overprinted with the Cenozoic normal fault and shear structures (Figure 2C,F).

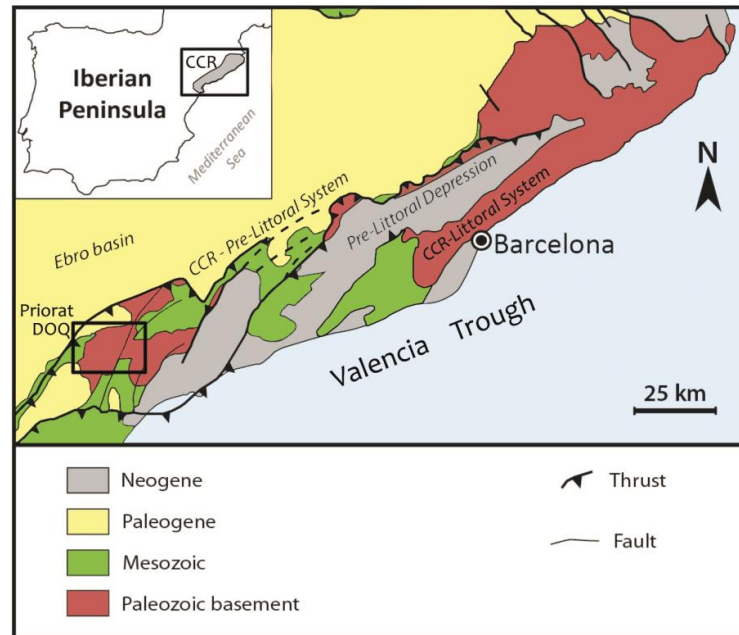


Figure 1. Tectonic setting of the Priorat DOQ region on the northeastern coast of the Iberian Peninsula. Geologic units and general tectonic outline of the Catalan Coastal Ranges are modified from [34].



Figure 2. Field relations in the Paleozoic basement of the Priorat DOQ region (CCR). (A) Part of the limb of a recumbent fault. Note Grenache vines on the left top of the outcrop. (B) Part of a small (~30 m) anticline fold. (C) Typical character of lava outcrop in the Priorat DOQ area overlain by black shale. (D) Interbedding of black shale and lithocrystalloclastic tuff. (E) Part of the limb of an overturned fold. (F) General nature of normal faulting in the Paleozoic basement emphasized by distribution of milky quartz selvages.

3. Methods

All mineralogical and geochemical studies were carried out at the Khabarovsk Innovative-Analytical Center (KhIAC) of the Institute of Tectonics and Geophysics of the Far East Branch of the Russian Academy of Sciences. Mineralogical studies were carried out using a VEGA 3 LMH TESCAN (Tescan, Brno, Czech Republic) scanning electron microscope (SEM) with an Oxford X-Max 80 Gb energy dispersive spectrometer (EDS) with the following operating conditions: accelerating voltage of 20 kV, beam current of 530 nA and beam diameter of 0.2 μm . A set of reference samples including 37 natural and synthetic oxides, minerals and pure native metals (Oxford/108699 no. 6067) were used as standards. Co-standard Oxford Instruments/143100 no. 9864-15 was used for daily calibration of the SEM instrument. Accuracy of the EDS analyses was estimated to be ± 0.1 wt.%

Major elements in black shale, volcanic and volcanoclastic rocks from the Priorat DOQ area were measured on pressed pellets using a S4 Pioneer XRF spectrometer (Bruker, Leipzig, Germany). International LDI-3 (gabbro) and WMG-1a (mineralized gabbro) reference materials were used for calibration. The analytical accuracy for major elements in the course of this study was $\pm 10\%$. Abundances of trace elements were determined with an ELAN 9000 ICP-MS (Perkin Elmer, Woodbridge, ON, Canada) after the acid digestion of a powdered sample. In addition to the above listed standards, geochemical reference samples BHVO-2 (USGS; Hawaiian basalt) and JB-3 (Geological Survey of Japan; Fuji basalt), along with Perkin Elmer standard solutions PE# N9300231-9300234 for internal calibration, were used to control the accuracy of analytical measurements. In the course of this study, the accuracy was $\pm 5\%$ for trace element abundances of >20 ppm and $\pm 10\%$ for chemical elements with abundances of <20 ppm [39]. Platinum-group elements (Ru, Rh, Ir, Pd, Pt) and Au were determined by ICP-MS after separation and pre-concentration by Na_2O_2 fire-assay and tellurium co-precipitation following the method described in [40]. Additional details of the analytical procedures used in the current study can be found in [39,41].

4. Results

As Paleozoic black shale is the principal source of “Ilicorella”, the world famous soil type underlying Priorat’s vineyards, we paid special attention to its mineralogical and geochemical features. Selected samples of black shale, mafic to intermediate lava and tuff, as well as volcanoclastic rocks (sandstone, shale) were analyzed for their major and trace element compositions to determine the possible paleotectonic environment of their formation.

4.1. Mineralogy of Black Shale

The Paleozoic black shale in the Priorat DOQ area is composed of amorphous carbonaceous matter (mostly graphite), volcanic-derived minerals (feldspar, mica, chlorite, amphibole), erosional material (mostly quartz), abundant framboidal aggregates of pyrite and magnetite (Figure 3) and other ore minerals, such as sphalerite (Figure 4), native and cupriferous silver (Figure 5), rare earth element (REE)-bearing phosphates (Figure 6) as well as zircon, baddeleyite and carbonate (calcite, siderite) minerals (Figure 7).

Pyrite forms discrete spheroidal crystals ranging from 1 to 10 μm in size, filling the void in the carbonaceous feldspar–quartz–chlorite–sericite matrix, frequently in association with calcite (Figure 3A). Pyrite framboids are very common (Figure 3B–D) and complex; occasionally distorted textural forms are also observed (Figure 3B,D). Individual pyrite crystals within voids (Figure 3A), polyframboids (Figure 3C) and distorted, irregular (sub-framboidal) structures (Figure 3B,D) typically display globular, cubic, octahedral and truncated-cubic crystalline shapes. Occasionally, pyrite framboids are associated with discrete tenorite (CuO) crystals (Figure 3B). In some samples, spheroidal magnetite crystals, either densely packed into framboid-like structures (Figure 3E), or localized in small (<50 μm) voids are present in the carbonaceous black shale matrix (Figure 3F).

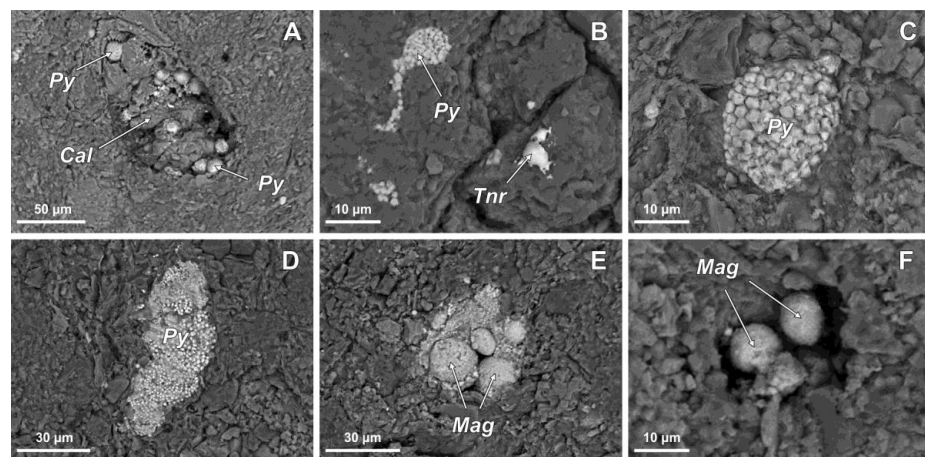


Figure 3. Framboidal Fe sulfide and oxide in Priorat black shale. (A) Development of discrete grains of framboidal pyrite within textural void filled with subhedral calcite crystals. (B) Framboidal pyrite in association with tenorite (CuO). (C) Single framboid composed of truncated-cubic and octahedral pyrite microcrystals. (D) Cluster (>60 μm) of densely spheroidal pyrite microcrystals (each ~1–2 μm across). (E) Individual spheroidal magnetite crystals. (F) Spheroidal magnetite crystals in a void in black shale. Py—pyrite, Mag—magnetite, Cal—calcite, Tnr—tenorite. All mineral abbreviations in Figures 3–7 are derived from [42].

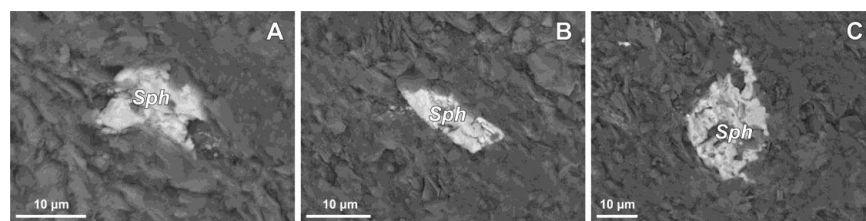


Figure 4. Occurrence of sphalerite (Sph) in black shale from the Priorat DOQ. (A) Cluster of small euhedral microcrystals. (B) Discrete euhedral sphalerite crystal. (C) Partially chemically abraded, equant sphalerite grain.

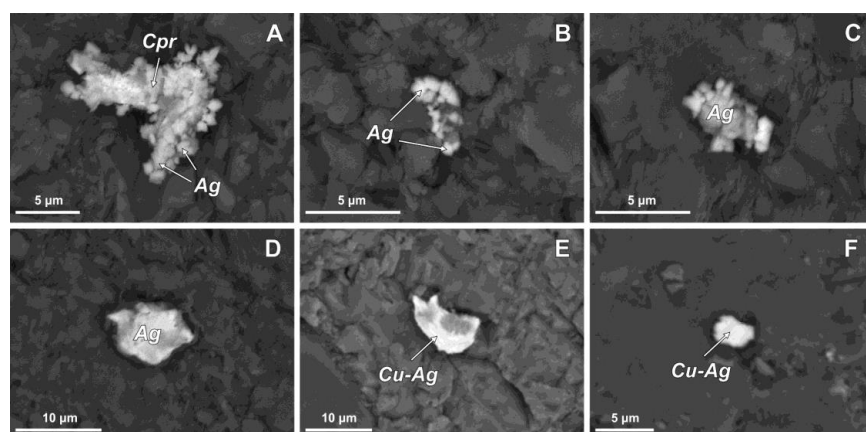


Figure 5. Occurrence of native and cupriferous silver in black shale from the Priorat DOQ. (A) Cluster of small (<10 μm) euhedral cuboid silver (Ag) microcrystals intergrown with cuprite (Cpr). (B) An aggregate of anhedral to subhedral silver grains in the feldspar-sericite matrix. (C) An aggregate of almost globular (less than 1 μm) silver (with minor Cl = 2.13 wt.%; chlorargyrite micro-inclusion?) microcrystals. (D) Discrete euhedral sub-equant cupriferous (Cu = 4.1 wt.%) silver (Cu–Ag) grain. (E) Cupriferous (Cu = 2.26 wt.%) silver film mantling feldspar (?) grain. (F) Euhedral equant cupriferous (Cu = 1.94 wt.%) silver (Cu–Ag) micro-crystal in carbonaceous matrix.

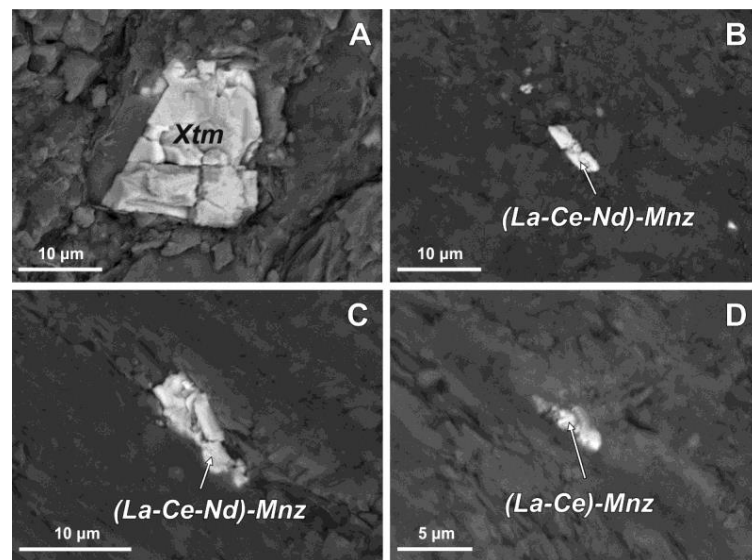


Figure 6. Rare earth element (REE)-bearing minerals in black shale from the Priorat DOQ region. (A) Euhedral xenotime (Xtm) crystal. (B) Elongated euhedral (La–Ce–Nd)-monazite (Mnz) crystal with 11.67 wt.% La, 17.68 wt.% Ce and 4.66 wt.% Nd. (C) Small aggregate of (La–Ce–Nd)-monazite microcrystals (La = 12.88 wt.%; Ce = 25.54 wt.%; Pr = 2.24 wt.%; Nd = 11.61 wt.%; also with 1.11 wt.% Ag and 0.71 wt.% Os). (D) Partially disintegrated or chemically abraded euhedral (La–Ce)-monazite microcrystal (La = 15.99 wt.%; Ce = 33.22 wt.%, Pr = 2.89 wt.%; Nd = 11.21 wt.%).

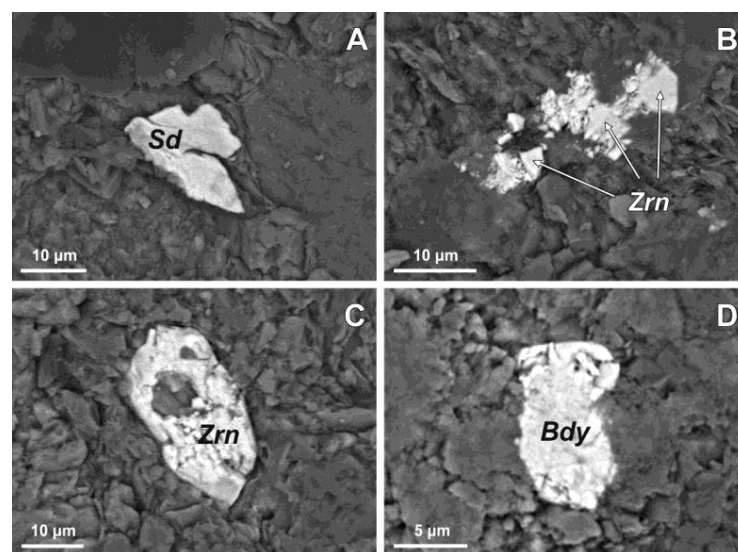


Figure 7. Occurrence of euhedral siderite (A), micro-aggregate (B) and larger euhedral crystal (C) of zircon, and euhedral baddeleyite (D) in black shale from the Priorat DOQ region. Sd—siderite, Zrn—zircon, Bdy—baddeleyite.

Sphalerite in black shale occurs mostly as clusters of euhedral to subhedral microcrystals (Figure 4A) and as discrete euhedral (Figure 4B), occasionally partially (chemically) abraded equant to sub-equant grains (Figure 4C).

Silver in black shale from the Priorat DOQ region is observed in a range of textural and compositional varieties (Figure 5). This precious chalcophile metal forms aggregates of euhedral cuboid (Figure 5A), anhedral equant (Figure 5B) and almost globular-like (Figure 5C) microcrystals, occasionally in association with cuprite (Figure 5A). Discrete euhedral cupriferous (Cu = 1–4 wt.%) silver microcrystals (Figure 5D,F), as well as thin (under 1 μm) films on silicate minerals (Figure 5E) are also quite common. Small amounts

of chlorine (~2 wt.% Cl) were detected in one densely packed cluster of native silver grains, possibly indicating the presence of either thin film or micro-inclusions of chlorargyrite (AgCl) composition (Figure 5C).

REE-bearing minerals are also present in the black shale from the Priorat DOQ region and are represented by euhedral xenotime (Figure 6A) and LREE-rich monazite with varying lanthanum (La = 10–16 wt.%), cerium (Ce = 17–33 wt.%), praseodymium (Pr < 3 wt.%) and neodymium (Nd = 4–12 wt.%) contents (Figure 6B–D). One monazite grain contains minor concentrations of silver (~1 wt.%) and osmium (~0.7 wt.%) (Figure 6C).

Other accessory minerals in black shale from the Priorat DOQ region include siderite (FeCO₃; Figure 7A), microcrystalline aggregates (Figure 7B) and discrete euhedral grains (Figure 7C) of zircon, as well as individual grains of euhedral baddeleyite (Figure 7D).

4.2. Geochemistry of Black Shale and Associated Volcanic Rocks

In addition to the dominant black shale lithology, Paleozoic sequences in the Priorat DOQ region include lava flows and possible sills of aphyric to scarcely porphyritic (mostly feldspar) mafic to intermediate compositions as well as lithocrystalloclastic felsic to intermediate tuffs and diverse volcanoclastic rocks (sandstone, siltstone, shale). Representative major (wt.%) and trace (ppm) element compositions of these volcano-sedimentary lithologies are listed in Tables 1–4.

Table 1. Chemical composition of Paleozoic black shale from the Priorat DOQ region (CCR).

Sample#	PR-1	PR-2	PR-3	PR-4	PR-9	PR-11	PR-14	PR-25	PR-26
SiO ₂ (wt.%)	55.35	54.43	53.31	53.03	66.00	66.87	75.62	69.81	82.08
TiO ₂	0.69	0.67	0.69	0.69	0.76	0.80	0.72	0.98	0.47
Al ₂ O ₃	8.35	8.60	8.72	8.72	14.58	15.18	12.62	11.33	9.17
Fe ₂ O ₃	4.63	4.37	4.45	4.43	7.13	5.72	3.96	8.15	2.12
MnO	0.03	0.03	0.03	0.03	0.07	0.08	0.05	0.07	0.09
MgO	0.95	0.96	0.97	0.96	2.71	2.86	0.50	1.32	0.80
CaO	13.84	15.09	15.55	15.89	0.56	0.53	0.63	0.68	0.20
Na ₂ O	0.64	0.59	0.62	0.60	1.06	1.74	1.46	0.53	0.57
K ₂ O	1.65	1.62	1.69	1.65	2.79	2.61	2.02	1.69	1.70
P ₂ O ₅	0.03	0.03	0.03	0.03	0.13	0.14	0.14	0.16	0.05
LOI	13.65	13.64	13.70	13.86	4.46	3.62	2.34	5.27	2.98
Total	99.81	100.03	99.76	99.87	100.26	100.15	100.06	99.99	100.23
ICV ¹	2.69	2.71	2.75	2.78	1.04	0.95	0.74	1.19	0.61
Li (ppm)	30.65	34.77	36.79	38.34	62.58	66.91	25.25	47.20	17.79
Sc	6.68	6.39	6.47	6.45	12.66	11.99	8.83	8.59	3.99
V	65.30	62.97	63.44	63.02	98.58	85.64	62.04	60.53	59.89
Cr	185.39	114.11	110.96	111.63	76.72	99.55	140.31	70.93	60.40
Co	11.56	9.54	9.79	9.28	24.55	16.89	16.94	21.41	14.93
Ni	37.61	31.34	32.94	30.07	31.93	31.85	27.18	50.34	31.71
Cu	125.51	25.31	50.32	32.18	54.46	25.13	21.80	13.45	90.45
Zn	64.34	45.48	43.12	30.30	516.63	135.88	53.43	73.21	23.35
Cs	5.61	5.06	5.16	7.72	7.23	3.40	2.48	8.37	3.74
Rb	62.19	58.57	59.45	58.00	113.90	94.32	83.14	69.24	66.43
Ba	125.98	114.65	118.64	110.57	492.07	761.88	359.22	220.41	177.13
Sr	388.56	416.23	403.21	427.23	79.84	86.79	47.23	49.76	34.49
Zr	53.01	46.23	44.74	45.34	80.23	74.75	58.93	88.63	53.01
Y	11.05	11.33	11.31	10.83	18.19	10.70	9.34	18.47	12.60
Nb	9.79	8.72	8.59	8.31	9.01	9.22	5.91	10.38	7.50
Ta	1.26	1.05	0.98	0.93	0.64	0.67	0.32	0.59	0.41
Hf	1.62	1.31	1.28	1.28	2.32	2.35	1.86	2.55	1.59
Th	6.90	6.32	6.08	6.05	9.19	9.99	8.91	7.70	6.11
U	8.99	7.85	8.02	7.73	2.02	1.54	1.53	1.57	1.34
Pb	14.07	11.48	10.99	10.99	337.91	30.22	7.81	14.00	8.23
La	16.76	14.70	13.79	14.05	28.83	34.23	25.63	19.38	18.26
Ce	39.49	35.79	34.41	34.28	67.66	73.08	59.23	44.42	36.45
Pr	4.51	4.10	3.96	2.89	7.02	7.57	6.15	4.77	3.56
Nd	16.99	15.43	14.97	15.25	29.54	30.67	25.24	21.41	13.61
Sm	3.38	3.27	3.14	3.20	6.33	5.76	4.77	4.92	2.44
Eu	0.65	0.63	0.62	0.62	1.20	0.98	0.85	1.12	0.61
Gd	3.61	3.39	3.31	3.31	6.42	5.33	4.60	5.33	3.15
Tb	0.48	0.46	0.45	0.45	0.73	0.54	0.47	0.65	0.37
Dy	2.53	2.38	2.34	2.39	2.02	2.75	2.42	3.84	2.33
Ho	0.47	0.46	0.45	0.45	0.68	0.43	0.39	0.64	0.42
Er	1.39	1.26	1.23	1.26	2.21	1.43	1.25	2.13	1.42
Tm	0.19	0.18	0.18	0.18	0.27	0.18	0.16	0.26	0.18
Yb	1.32	1.17	1.11	1.16	2.00	1.40	1.22	1.94	1.32
Lu	0.19	0.17	0.16	0.17	0.26	0.19	0.16	0.26	0.18

¹ ICV (index of compositional variation) = (Fe₂O₃+K₂O+Na₂O+CaO+MgO+MnO+TiO₂)/Al₂O₃ [43].

Table 2. Chemical composition of Paleozoic volcanoclastic sediments from the Priorat DOQ region (CCR).

Sample#	PR-13	PR-16	PR-18	PR-22	PR-24	PR-28
SiO ₂ (wt.%)	69.18	69.66	66.92	70.87	70.96	72.07
TiO ₂	0.79	0.64	0.80	0.80	0.71	0.81
Al ₂ O ₃	12.83	11.01	14.50	14.51	15.05	14.11
Fe ₂ O ₃	5.49	3.62	5.18	4.70	3.96	4.58
MnO	0.10	0.13	0.11	0.05	0.07	0.08
MgO	2.32	1.83	1.42	1.35	1.27	1.03
CaO	1.87	4.10	2.11	0.37	0.44	0.36
Na ₂ O	1.63	2.15	2.12	1.66	2.40	2.17
K ₂ O	1.65	1.25	2.46	2.82	2.10	2.09
P ₂ O ₅	0.11	0.13	0.14	0.14	0.14	0.14
LOI	4.18	5.59	4.34	2.85	3.10	2.63
Total	100.13	100.11	100.09	100.13	100.19	100.07
ICV ¹	1.08	1.25	0.98	0.81	0.73	0.79
Li (ppm)	44.34	21.04	29.97	26.47	19.80	17.00
Sc	11.39	7.41	11.49	10.12	8.84	8.48
V	75.12	56.96	85065	77.75	68.03	61.09
Cr	133.73	116.01	114.54	110.27	119.17	109.03
Co	13.45	14.87	20.38	16.25	12.77	14.26
Ni	32.09	19.73	29.25	25.58	22.80	21.95
Cu	18.49	15.55	39.18	22.27	24.00	25.98
Zn	110.14	38.72	52.78	294.42	71.58	55.14
Cs	5.16	1.66	3.50	3.29	4.58	3.71
Rb	81.55	44.01	85.50	91.98	70.40	60.13
Ba	578.85	378.53	436.95	430.16	366.61	330.66
Sr	182.94	68.92	71.58	51.04	87.88	85.71
Zr	59.05	60.83	63.05	98.52	48.98	44.50
Y	16.31	14.74	10.81	13.15	9.20	13.87
Nb	7.73	4.68	5.80	8.18	6.56	6.07
Ta	0.50	0.28	0.39	0.50	0.37	0.37
Hf	1.77	1.66	1.94	1.92	1.39	1.34
Th	7.68	6.76	7.89	7.21	4.96	5.31
U	1.13	1.34	1.77	1.38	1.21	1.17
Pb	25.30	3.93	4.85	126.67	5.93	7.47
La	22.39	23.23	25.77	27.61	19.41	19.78
Ce	54.73	52.22	60.21	64.69	46.48	43.21
Pr	5.25	5.48	6.08	6.58	4.80	4.65
Nd	21.75	22.85	25.68	27.11	20.44	20.54
Sm	4.38	4.59	5.05	5.28	4.08	4.08
Eu	0.95	0.91	1.02	0.98	0.82	0.87
Gd	4.67	4.64	4.91	5.03	3.79	4.11
Tb	0.59	0.52	0.52	0.57	0.39	0.48
Dy	3.52	2.96	2.76	3.05	2.08	2.87
Ho	0.59	0.48	0.45	0.51	0.36	0.50
Er	1.95	1.58	1.40	1.63	1.24	1.69
Tm	0.24	0.19	0.18	0.21	0.19	0.21
Yb	1.81	1.49	1.34	1.57	1.17	1.54
Lu	0.23	0.19	0.18	0.21	0.16	0.20

¹ ICV (index of compositional variation) = (Fe₂O₃+K₂O+Na₂O+CaO+MgO+MnO+TiO₂)/Al₂O₃ [43].

Table 3. Chemical composition of Paleozoic lavas from the Priorat DOQ region (CCR).

Sample#	PR-5	PR-10	PR-19	PR-20	PR-23	PR-27
SiO ₂ (wt.%)	56.07	56.35	51.51	53.93	55.54	55.73
TiO ₂	0.97	0.90	1.18	0.99	1.00	0.95
Al ₂ O ₃	18.30	17.96	21.44	20.28	18.76	19.65
Fe ₂ O ₃	8.83	8.32	7.73	7.75	8.21	7.97
MnO	0.05	0.09	0.06	0.05	0.08	0.08
MgO	3.45	3.83	3.69	3.64	2.99	2.28
CaO	0.82	0.68	0.70	0.62	0.66	0.70
Na ₂ O	1.01	0.98	0.77	1.14	1.27	0.79
K ₂ O	4.90	4.41	5.98	5.01	4.28	4.97
P ₂ O ₅	0.18	0.16	0.15	0.14	0.15	0.12
LOI	5.33	6.50	7.17	6.68	7.10	7.05
Total	99.89	100.16	100.39	100.24	100.03	100.30
Li (ppm)	80.47	91.37	31.23	40.29	62.39	36.09
Sc	17.67	17.16	22.38	18.44	21.19	16.89
V	146.41	148.27	177.06	146.17	166.63	129.54
Cr	128.27	103.95	119.58	110.99	133.11	99.29
Co	20.90	13.46	13.23	14.73	19.57	17.88
Ni	63.28	40.16	47.10	49.22	51.85	46.25
Cu	235.90	22.06	33.37	29.23	44.09	40.60
Zn	166.31	122.03	82.59	310.43	123.60	117.92
Cs	7.72	9.18	9.26	6.95	11.62	7.28
Rb	141.16	169.64	237.32	199.84	174.23	192.97
Ba	824.35	761.88	1068.64	771.93	729.26	873.86
Sr	43.93	65.38	68.64	84.49	82.72	87.39
Zr	97.65	126.16	118.08	93.67	98.52	78.85
Y	15.91	25.29	17.17	19.41	17.84	22.76
Nb	21.21	14.87	7.73	12.53	11.26	8.12
Ta	2.79	1.30	0.56	0.84	0.67	0.51
Hf	2.83	3.33	2.99	2.65	2.90	2.32
Th	15.17	14.38	13.74	13.73	13.59	12.15
U	10.23	2.42	2.76	2.21	2.92	1.65
Pb	27.89	24.25	7.67	25.79	22.03	23.81
La	45.31	37.33	47.53	47.26	42.10	44.18
Ce	94.90	49.98	100.08	97.80	90.99	84.57
Pr	10.77	8.24	9.92	9.88	9.35	9.50
Nd	38.62	33.86	40.46	40.84	38.89	39.05
Sm	6.96	6.94	7.80	7.73	7.81	7.61
Eu	1.58	1.42	1.50	1.44	1.54	1.38
Gd	7.04	7.18	7.31	7.27	7.68	7.48
Tb	0.82	0.90	0.78	0.78	0.84	0.90
Dy	3.90	5.35	4.07	4.40	4.53	5.21
Ho	0.67	0.94	0.66	0.71	0.72	0.86
Er	1.94	3.04	2.30	2.41	2.29	2.92
Tm	0.27	0.39	0.30	0.31	0.29	0.36
Yb	1.98	2.86	2.43	2.35	2.20	2.73
Lu	0.31	0.38	0.34	0.31	0.30	0.35

Black shale of the Priorat DOQ area includes two principal compositional groups (Table 1): (1) the low SiO₂ and Al₂O₃ (52–54 wt.% and ~8 wt.%, respectively), high CaO (13–16 wt.%) and (2) high SiO₂ and Al₂O₃ (66–82 wt.% and 9–15 wt.%, respectively), very low CaO (<1 wt.%). Both groups are characterized by variable MgO contents (0.5–2.8 wt.%) and general potassic character (K₂O/Na₂O > 1; Table 1). All black shale lithologies are enriched in Cs, Rb and U and light rare earth elements (LREE) and depleted in high-field strength elements (HFSE), such as Nb, Ta, Zr and Hf (Figure 8). High-Ca, low-Si-Al black shale is also slightly enriched, while siliceous low-Ca black shale is strongly depleted in Sr

(Figure 8). REE compositions are also characterized by weak negative Eu and Tm anomalies (Figure 8).

Table 4. Chemical composition of Paleozoic tuffs from the Priorat DOQ region (CCR).

Sample#	PR-6	PR-7	PR-8	PR-12	PR-15	PR-17	PR-21
SiO ₂ (wt.%)	68.57	67.24	67.06	66.08	56.99	61.91	67.72
TiO ₂	0.67	0.72	0.78	0.68	0.47	0.79	0.82
Al ₂ O ₃	11.37	13.86	15.34	13.32	19.32	16.80	14.29
Fe ₂ O ₃	5.95	4.85	4.62	6.45	3.98	7.45	5.05
MnO	0.12	0.08	0.06	0.11	0.08	0.08	0.05
MgO	3.78	3.86	2.92	2.87	0.31	2.12	2.23
CaO	1.43	0.80	0.59	1.85	1.30	1.14	0.46
Na ₂ O	1.21	1.30	1.24	0.72	15.01	1.52	2.37
K ₂ O	4.28	2.54	3.57	1.90	0.24	2.95	2.13
P ₂ O ₅	0.15	0.12	0.15	0.10	0.12	0.17	0.16
LOI	2.62	4.66	3.80	6.10	2.40	5.30	4.90
Total	100.16	100.03	100.13	100.17	100.23	100.23	100.18
Li (ppm)	80.28	47.78	44.65	73.24	30.01	35.80	32.88
Sc	11.24	10.68	12.09	11.90	6.96	13.10	12.27
V	82.54	78.80	92.23	76.67	59.17	104.69	94.89
Cr	114.22	105.12	120.46	94.17	72.49	92.04	117.75
Co	23.37	11.32	14.85	19.32	17.67	18.46	16.21
Ni	22.90	29.43	27.79	38.26	29.10	37.25	32.62
Cu	18.72	17.37	16.91	20.56	14.82	26.76	12.78
Zn	394.38	96.37	81.62	137.60	37.10	74.58	72.06
Cs	1.95	6.80	7.30	8.05	0.45	4.56	2.84
Rb	111.26	95.89	134.20	110.00	7.72	110.10	70.19
Ba	1364.91	492.07	507.98	800.62	88.44	586.79	397.65
Sr	196.31	58.19	51.74	105.72	318.09	85.82	79.15
Zr	70.67	76.05	82.80	55.79	59.38	83.22	79.80
Y	20.60	18.25	19.27	18.19	9.57	14.05	13.14
Nb	11.60	8.48	10.05	9.62	4.87	8.44	7.36
Ta	0.76	0.49	0.62	0.65	0.43	0.53	0.47
Hf	2.01	2.19	2.32	1.69	1.77	2.26	2.27
Th	9.49	9.13	10.90	8.32	7.72	9.94	8.09
U	1.80	1.28	1.71	1.23	1.55	2.09	1.59
Pb	163.23	36.68	29.53	58.57	5.36	10.75	3.97
La	28.82	28.46	35.12	20.11	19.01	39.78	27.75
Ce	63.68	62.47	72.80	52.75	43.75	82.57	62.64
Pr	6.81	6.45	7.92	4.97	4.42	8.38	6.45
Nd	27.20	25.66	31.30	20.27	18.30	35.33	26.81
Sm	5.44	5.05	6.04	4.37	3.58	7.10	5.36
Eu	1.43	0.95	1.14	1.19	0.74	1.35	1.16
Gd	5.96	5.28	6.31	4.76	3.71	6.45	5.39
Tb	0.75	0.64	0.75	0.61	0.40	0.66	0.59
Dy	4.24	3.73	4.13	3.90	2.31	3.45	3.30
Ho	0.76	0.66	0.72	0.68	0.40	0.54	0.57
Er	2.33	2.11	2.32	2.23	1.31	1.80	1.87
Tm	0.28	0.27	0.30	0.29	0.16	0.22	0.24
Yb	1.96	1.90	2.04	2.09	1.22	1.73	1.75
Lu	0.27	0.25	0.27	0.26	0.17	0.22	0.24

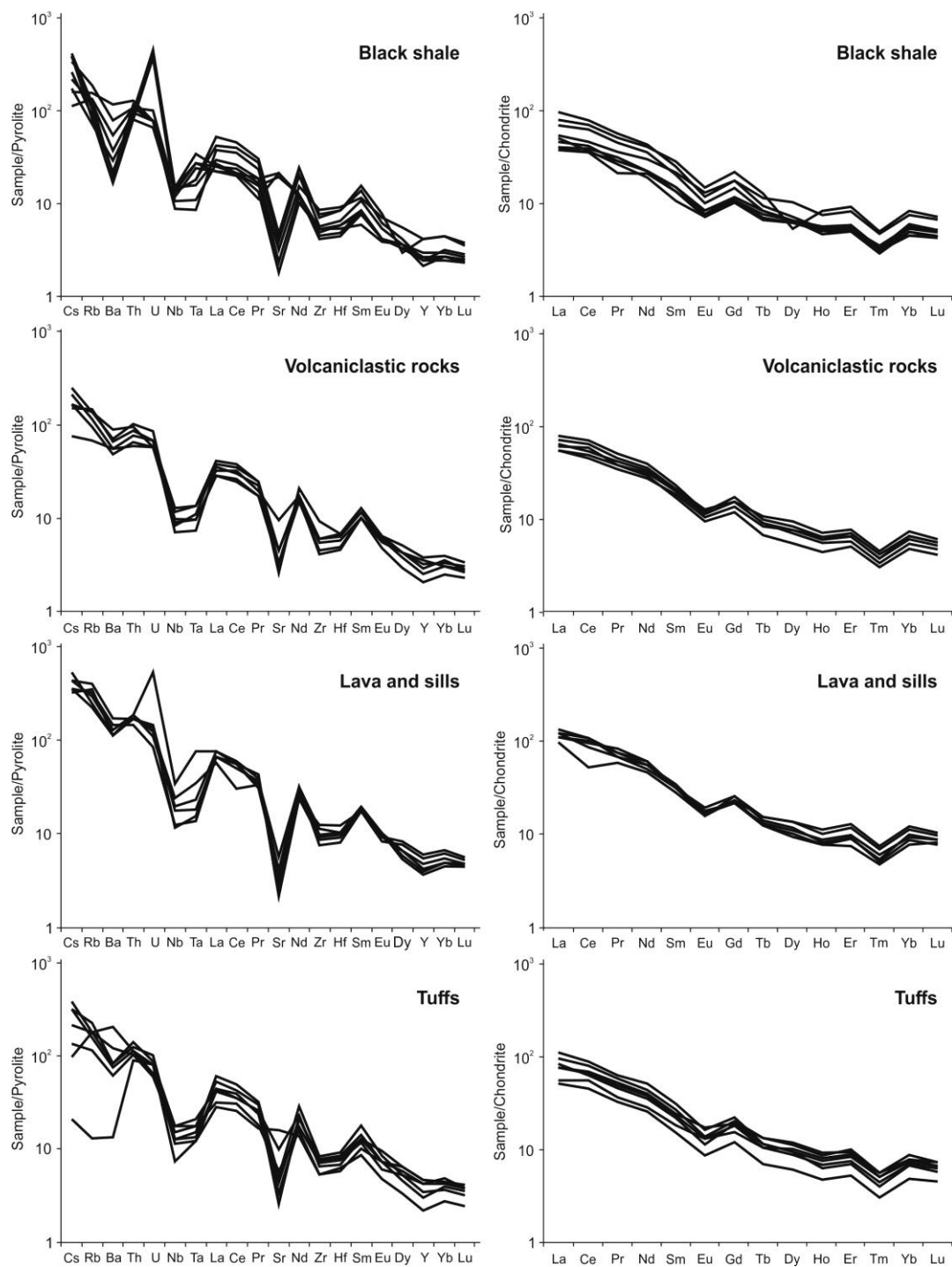


Figure 8. Primitive mantle (pyrolite)-normalized trace element (**left column**) and chondrite-normalized rare earth element (REE) (**right column**) patterns for volcanic (lava, sills and tuffs) and volcano-sedimentary (black shale and volcaniclastic sediments) rocks from the Priorat DOQ region (CCR). Normalizing values for pyrolite are from [43], for ordinary chondrite—from [44].

Volcaniclastic sedimentary rocks from the Priorat DOQ region (sandstone, mudstone, siltstone, shale) display Si- and Al-rich major element compositions ($\text{SiO}_2 = 66\text{--}72$ wt.%; $\text{Al}_2\text{O}_3 = 11\text{--}15$ wt.%; Table 2) with elevated MgO (1–2 wt.%) and variable CaO (0.3–4 wt.%; Table 2) contents and $\text{K}_2\text{O}/\text{Na}_2\text{O}$ ratios ranging from 0.6 to 1.7. Volcaniclastic sediments are clearly enriched in all large-ion lithophile elements (LILE), such as Cs, Rb, Ba and U, and depleted in HFSE (Nb, Ta, Ti, Zr and Hf; Figure 8). Most sandstone and

shale/mudstone/siltstone samples also display profound negative Sr anomaly and are characterized by LREE enrichment in chondrite-normalized rare earth element patterns (Figure 8).

Paleozoic lava flows and sills from the Priorat DOQ region are characterized by basaltic to basaltic andesite silica contents (51.5–55.7 wt.%), high Al₂O₃ (17.9–21.4 wt.%), low CaO and Na₂O (both <1.3 wt.%) and elevated K₂O (4–6 wt.%; Table 3). High K₂O/Na₂O ratios of 3.4 to 7.8 identify volcanic rocks from the Priorat DOQ region as derivatives (fractionates) of primary potassic (shoshonitic/absarokitic) magmas (typically characterized by K₂O/Na₂O ratios of >1; [45,46]). Volcanic rocks from Priorat display strong LILE (Cs = 6.95–11.62 ppm, Rb = 141–237 ppm, Ba = 729–1068 ppm; Table 3), LREE and Th (12–15 ppm; Table 3) enrichments, coupled with pronounced HFSE (especially, Nb and Ta) depletions (Figure 8). Negative Sr anomalies characteristic of Priorat sediments are also present in Paleozoic lavas and sills (Figure 8). One potassic lava sample also displays a weak but identifiable negative Ce-anomaly, possibly indicative of pelagic sediment recycling in magma sources of Priorat potassic volcanic rocks [47–49].

Lithocrystalloclastic tuffs that accompany potassic lavas and sills or form individual horizons (typically several centimeters to 0.5 m thick) within the Paleozoic Priorat sequence are characterized by substantial variations in SiO₂ (56–68 wt.%), Al₂O₃ (11–19 wt.%), CaO (0.46–1.85 wt.%) and MgO (0.31–3.86 wt.%) contents (Table 4). One tuff sample (PR-15; Table 4) displays a highly anomalous Na₂O content of ~15 wt.% (possibly caused by intense metasomatic zeolitization of this sample), while K₂O/Na₂O ratios (1–3) in other pyroclastic samples identify them as members of the potassic igneous series [45,46]. Although LILE concentrations in Priorat tuffs are quite variable (Table 4), most probably due to spotty hydrothermal alteration (very common in highly porous and permeable pyroclastic rocks), well-pronounced HFSE depletions and LREE enrichments are almost identical to potassic lavas and, to a certain degree, to black shale and volcanoclastic sediment compositions from the Priorat DOQ region (Figure 8).

Concentrations of platinum-group elements (PGE) and gold in four samples of the black shale (PR-1, PR-2, PR-3, PR-4) and one potassic lava flow (PR-5) are presented in Table 5.

Table 5. Concentrations and selected inter-element ratios of platinum-group elements (PGE) and Au (ppb) in Paleozoic black shale and lava flow from the Priorat DOQ region (CCR).

Sample#	PR-1	PR-2	PR-3	PR-4	PR-5
Lithology	Black Shale	Black Shale	Black Shale	Black Shale	Lava Flow
Ru	0.24	0.28	0.27	0.28	0.34
Rh	<0.001	0.36	0.05	0.07	0.11
Ir	<0.001	<0.001	<0.001	0.15	0.25
Pd	<0.001	<0.001	<0.001	<0.001	0.01
Pt	0.55	1.58	1.38	0.88	1.24
Au	87.17	1161.28	132.26	140.24	147.32
Au/Pt	158.5	735.0	95.9	159.4	118.8
Au/Ru	363.2	414.7	489.9	500.9	433.3
Pt/Ru	2.29	5.64	5.11	3.14	3.65
Pt/Ir				5.87	4.96
Au/Ir				934.9	589.3
Pt/Rh		4.39	27.6	12.6	11.27
Au/Rh		3225	2645	2003	1339
Ru/Ir				1.87	1.36
Rh/Ir				0.45	0.44

Black shale samples show high to very high (up to 1161 ppb; Table 5) concentrations of gold and elevated platinum concentrations (0.55–1.58 ppb; Table 5), along with very low concentrations of palladium and most elements of the Ir-group (Ir, Rh, Ru). In fact, Pd is below the detection limit of 0.001 ppb in all black shale samples and Ir—in 3 samples,

except one (PR-4, Ir = 0.15 ppb; Table 5). This is consistent with PGE concentrations and behavior reported for Phanerozoic black shale formations worldwide [44]. High Au/Pt, Au/Ru, Au/Rh and Au/Ir ratios in Priorat black shale suggest clear Au enrichments over refractory Ir-group PGEs and Pt (Table 5). The Ir-group metals are only weakly fractionated (Ru/Ir = 1.87, Rh/Ir = 0.44 in sample PR-5; Table 5), which is typical of immature black shale formations in the Phanerozoic [44]. The potassic lava flow (sample PR-5 in Table 5) is also characterized by elevated Au (1161 ppb) and, to a lesser extent, Pt (1.24 ppb) concentrations and obvious Au enrichment in reference to the PGEs (Au/Pt = 118.8, Au/Ru = 433, Au/Ir = 589, Au/Rh = 1339; Table 5). Inter-element ratios within the Ir-group PGEs (e.g., Ru/Ir = 1.36, Rh/Ir = 0.44) point to only weak fractionation among the refractory PGEs, quite similar to the black shale sample PR-4 (Ru/Ir = 1.87, Rh/Ir = 0.45; Table 5). Strong Au enrichment over refractory PGEs (Au/Ru > 300, Au/Rh > 2000, Au/Ir > 900; Table 5) is observed in all black shale samples from the Priorat DOQ region.

5. Discussion

The results of our field, mineralogical and geochemical study of Paleozoic rocks associated with the wine-growing industry in the Priorat DOQ region suggest that they are composed of predominant black shale lithology with subordinate volcanoclastic sandstone and shale interbedded with shoshonitic lava flows, thin (under 1 m) sills and lithoclastoclastic tuffs. All Paleozoic formations are folded into medium-scale (tens of meters) asymmetrical, overturned and recumbent folds (Figure 2A,B,E), commonly affected to various degrees by a later-stage brittle deformation (mostly normal faulting; Figure 2C,F). Based on the available data, we can draw some inferences on the sources and possible geodynamic environment of formation of the Paleozoic structural basement in the Catalan Coastal Ranges (CCR), with some implications for the tectonic setting and volcanic origins of the Priorat DOQ wine terroir.

5.1. Geochemical Constraints on the Nature of the Paleozoic Basement of the Catalan Coastal Ranges (SE Spain)

Geochemical data have been traditionally successfully used to determine the possible sources and provenance of various (including strongly hydrothermally altered or metamorphosed) sedimentary formations as well as paleotectonic setting and geodynamic significance of volcanic sequences of different age [41,43,46,50–62]. Major (K₂O–Na₂O–SiO₂) variations in black shale and volcanoclastic sediments from the Priorat DOQ region suggest their accumulation within a classic active continental margin setting, with three black shale samples plotting into the field of passive margin sediments (Figure 9A). Both black shale and volcanoclastic sandstone from Priorat plot into the field of continental island arc sediments on the triangular Th–La–Sc diagram (Figure 9B) of Bhatia and Crook [50].

Co-variation of Th/Sc and Zr/Sc ratios in the Priorat sediments suggest that their trace element compositions are close to average upper continental crust, are relatively immature and primarily derive from the erosion of arc-related andesitic, dacitic and rhyolitic sources (Figure 9C). This suggestion is confirmed by the variation of Co/Th and La/Sc ratios, with Priorat sediments plotting above the discrimination line between immature mafic and mature felsic sources (Co/Th = 1.27) and the generally transitional (basalt/andesite to dacite/rhyolite) geochemical nature (Figure 9D). Black shale and volcanoclastic samples from Priorat generally have La/Sc ratios of under 3–3.5 (similar to arc-derived turbidites), while sediments from passive margins usually have La/Sc ratios greater than 4 [51,63]. Similar compositional trends are observed in the La/Th versus Hf graph (Figure 9E), where Priorat sediments plot in the transitional area between andesitic and felsic arc sources at low La/Th (< 5) ratios typical of oceanic arc-derived turbidites [51,63,64]. Co-variation of TiO₂ (wt.%) and Ni (ppm) in Priorat sediments also identifies them as derivatives of felsic erosional sources with general immature compositional characteristics (Figure 9F). It is important to emphasize here that all sedimentary and volcanoclastic rocks from the Priorat DOQ area display pronounced negative HFSE (Nb, Ta, Zr, Hf, Ti) anomalies in

primitive mantle-normalized patterns (Figure 8), which (HFSE depletion) is globally a single most important geochemical characteristic of subduction-related (island arcs and active continental margins) tectonic settings [65–67]. Needless to say, most clastic sediments (turbidites, deep-sea sands, etc.) in forearc, intra-arc and back-arc depositional basins are characterized by distinct and unequivocal negative HFSE anomalies in mantle-normalized, multi-element patterns [62,64,68,69]. All the geochemical data presented above point to the formation of Priorat black shale and volcanoclastic sediments within a Paleozoic active continental margin similar in sedimentation style and geochemistry to modern day island arc-back arc configurations of the West Pacific region [64,68–72]. Primary sources of clastic material in the Priorat sediments appear to be of intermediate to felsic composition, such as evolved arc-related volcanic and plutonic complexes.

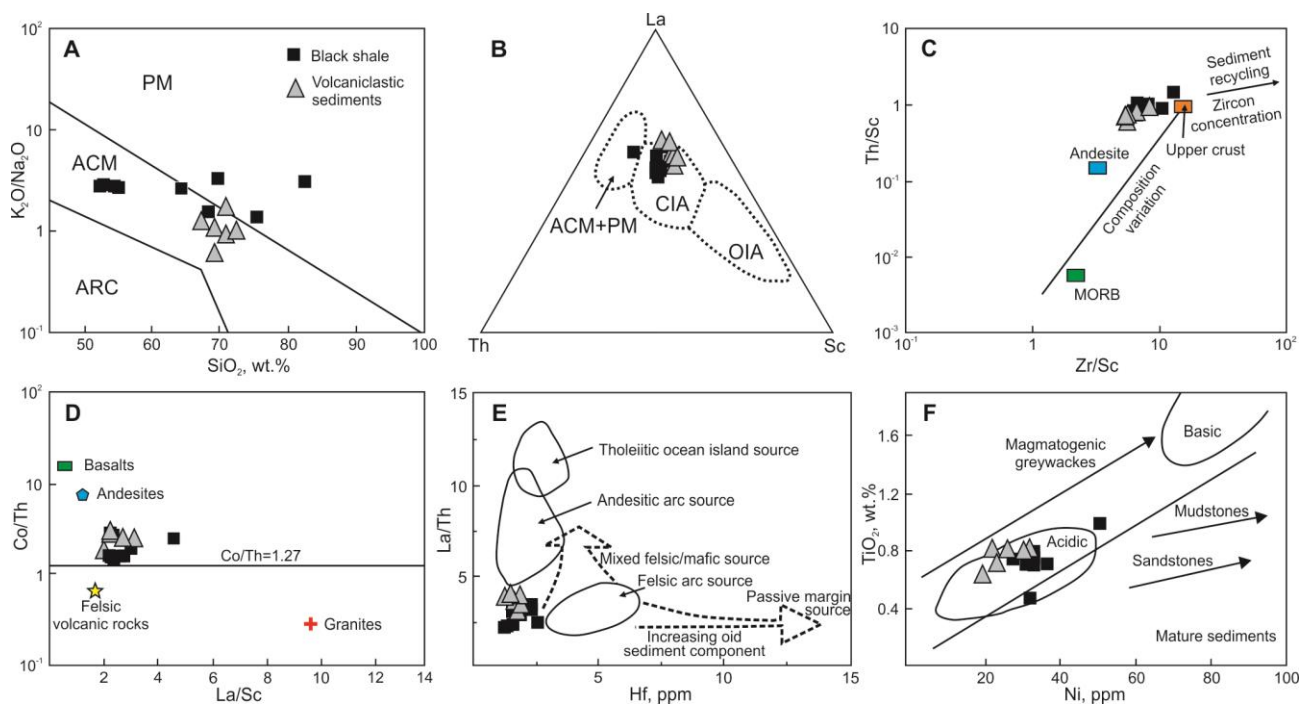


Figure 9. Source, provenance and tectonic interpretation diagrams for sedimentary rocks from the Priorat DOQ region. (A) SiO₂ (wt.%) vs. K₂O/Na₂O; fields of oceanic island arc (ARC), active continental margin (ACM) and passive margin (PM) sediments are from [50]. (B) Th–La–Sc graph; fields for oceanic island arc (OIA), continental island arc (CIA), active continental margin (ACM) and passive margin (PM) sediments are from [51]. (C) Th/Sc vs. Zr/Sc graph; average compositions of mid-ocean ridge basalt (MORB), andesite, upper continental crust and chemical trends are from [52]. (D) Co/Th vs. La/Sc; average compositions of various source rocks for clastic sediments are from [53]. (E) La/Th vs. Hf (ppm); compositional fields and principal chemical trends are from [54]. (F) Ni (ppm) vs. TiO₂ (wt.%); sediment sources and main compositional trends are from [55].

Geodynamic setting and magma sources for potassic lava flows, sills and tuffs that intercalate with black shale and volcanoclastic sediments in the Priorat DOQ region can be constrained using the set of tectonic discrimination diagrams presented in Figure 10. Potassic lavas and sills belong to the shoshonitic volcanic series on the basis of K₂O–SiO₂ relationships (Figure 10A). Tuffs plot into either high-K or normal calc-alkaline fields in the K₂O–SiO₂ classification plot of Peccerillo and Taylor [56], together with geographically proximal black shale and volcanoclastic sediment compositions (Figure 10A). Co-variation of K₂O and Na₂O classifies all volcanic samples and half of pyroclastic and black shale samples as ultrapotassic, while volcanoclastic sediments plot into the shoshonitic field (Figure 10B) and are compositionally similar to extension-related shoshonites from the Aegean Sea region [57,73,74]. TiO₂–SiO₂–K₂O systematics in Priorat potassic volcanic

rocks also emphasizes their transitional character between subduction-(arc)-related and extension-(rift)-related shoshonite magma series based on the classification proposed in [58] (Figure 10C). Priorat potassic rocks as well as spatially and structurally associated sediments plot into the field of shoshonite magmas in the Th/Yb–Nb/Yb diagram, exhibiting elevated E-MORB-like Nb/Yb and OIB-like Th/Yb inter-element ratios (Figure 10D). Similar geochemical characteristics in Tertiary shoshonite intrusives of eastern Tibet were interpreted as a result of partial melting of continental crust, subducted deep into the lithospheric mantle under transpressional, possibly leaky, fault regime [75]. As shown earlier for enriched shoshonitic lavas and intrusives in Kamchatka [58], Eastern Pontides continental arc in NE Turkey [76], the Sezia Zone in the Western Italian Alps [77] and various locations (Corsica, Murcia-Almeria in SE Spain, southern Tuscany) in the Western Mediterranean Region [78], identical geochemical signatures can be equally easily produced via the partial melting of veined mantle source composed of variably depleted mantle contaminated (metasomatized) by small-fraction siliceous melt from subducted pelagic (presumably, related to earlier subduction episodes). It is critically important to mention here that, in all these cases, enriched shoshonite magmas are associated with extensional tectonic regimes, such as frontal arc, intra-arc and back-arc rifts [57,58,73,74,76–79]. This is generally consistent with a broadly defined Andean-type continental arc geodynamic setting indicated by the Th/Yb–Ti/V systematics (Figure 10E). Paleozoic lavas, sills and pyroclastics from the Priorat DOQ region display low (typically < 2) Nb/Th ratios characteristic of subduction-related magmas [47,59,61,65,80,81]. On the other hand, low Zr/Nb ratios (< 10) in some volcanic samples from the Priorat region are comparable with OIB-like values [41,44,60,61]. This chemical characteristic may be reflective of mantle-melt metasomatic reactions in post-orogenic, shoshonite-producing mantle, or indicate a growing influence of mantle plume components interacting with subduction-modified post-collisional lithosphere [41,61,68,76,78].

Geochemical data suggest that Paleozoic sediments (black shale and volcanoclastic sandstone/mudstone/siltstone) and volcanic rocks (lavas, sills, tuffs) from the Priorat DOQ region were formed within the rifted (extended) Andean-type active continental margin. The presence of sills within the Paleozoic sedimentary sequence and general structural pattern of the Paleozoic basement of the Catalan Coastal Ranges (CCR) in the Priorat region is comparable with the sill-sediment complexes previously described in such classic extensional environments as the Gulf of California (essentially a young spreading center; [82]), the Faroe-Shetland Basin [83] and the sedimented slow-spreading Andaman Sea [84]. Extensional processes responsible for the generation of shoshonite melts within Andean-type active continental margins can occur in the frontal arc, intra-arc or back-arc geodynamic environment over a broad width of well-developed subduction-related arc-basin systems [41,58,72–74,76,78,85,86]. Based on specific structural features, stratigraphy and regional tectonic evolution of the Paleozoic basement of the CCR [35–38,87,88], as well as our new geologic, mineralogical and geochemical data from the Priorat DOQ region, we suggest that Paleozoic sequences (at least in the southern and central portion of the CCR) were formed in moderate to deep (in terms of water depth) back-arc or intra-arc, partially anoxic (ubiquitous presence of black shale with framboidal pyrite and Fe-oxides; Figure 3) basins within a rifted Andean-type active continental margin. Back-arc and intra-arc extension in the Paleozoic was accompanied by the formation of sill-sediment complexes indicative of early stages spreading-type tectonic processes as well as prolific shoshonitic magmatism similar (at least geochemically) to the Aegean Sea region, Kamchatka and the Western Mediterranean region. Although shoshonite magmas in the CCR are characterized by subduction-related geochemistry (high LILE and LREE contents, pronounced HFSE depletions), some trace element indicators (e.g., Th/Yb and Zr/Nb ratios; Figure 10) suggest potential involvement of plume-type (OIB-like) material. In addition, elevated (11–21 ppm; Table 3) Nb concentrations in some potassic lavas and sills from the Priorat region are comparable with those in high-Nb basalts in volcanic arcs worldwide [89,90]. Some of these

high-Nb basalt magmas are believed to be derived from a depleted mantle wedge source in subduction zones metasomatized by siliceous, high Sr/Y adakite melts [91–93].

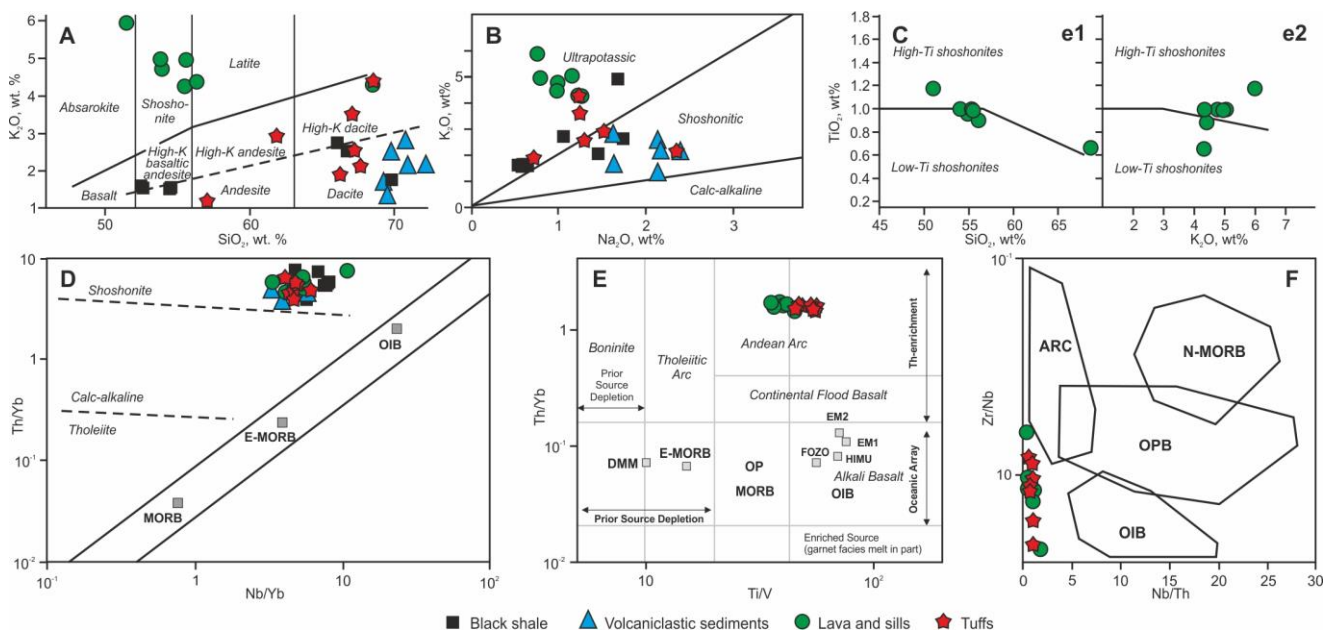


Figure 10. Geochemical systematics of volcanic (lava, sills and tufts) and volcanic-sedimentary (black shale and volcaniclastic sediments) rocks from the Priorat DOQ region. (A) SiO_2 (wt.%) vs. K_2O (wt.%). Fields for shoshonite, high-K and normal calc-alkaline volcanic rocks are derived from [56]. (B) K_2O (wt.%) vs. Na_2O (wt.%). Fields for ultrapotassic, shoshonitic and calc-alkaline volcanic series are modified from [57]. (C) TiO_2 (wt.%) vs. SiO_2 (wt.%) (e1) and TiO_2 (wt.%) vs. K_2O (wt.%) (e2) tectonic discrimination diagrams for shoshonite magma series. Compositional fields for high-Ti (rift-related, late- or post-orogenic) and low-Ti (arc-related) shoshonites are derived from [58]. (D) Th/Yb vs. Nb/Yb . Mantle array, average values for depleted mid-ocean basalt (N-MORB), enriched mid-ocean ridge basalt (E-MORB), oceanic island basalt (OIB) and fields for tholeiite, calc-alkaline and shoshonite magma series are derived from [59]. (E) Th/Yb vs. Ti/V . All compositional fields are derived from [60]. Average values for depleted mid-ocean ridge mantle source (DMM), enriched mid-ocean ridge basalt (E-MORB) and various enriched mantle components (EM1, EM2, HIMU, FOZO) follow the nomenclature of [41] and references therein. OIB—oceanic island basalts, OP MORB—oceanic plateau mid-ocean ridge basalt. (F) Zr/Nb vs. Nb/Th . Fields for island arc basalts (ARC), depleted (normal) mid-ocean ridge basalts (N-MORB), ocean plateau basalts (OPB) and ocean island basalts (OIB) are derived from [61].

5.2. Tectonic Setting and Volcanic Origins of the Priorat DOQ Wine Terroir

Paleozoic volcano-sedimentary formations underlie extensive, Grenache-dominated vineyards and provide a major source for a thriving wine industry in the Priorat DOQ region, with such wineries as Álvaro Palacios, Clos Erasmus, Clos Martinet, Clos de l’Obac, Clos Galena and Clos Figueras being world famous for their exceptional quality grand cru-style wines. The main source of world-class wines in Priorat is “llicorella”—a type of dark-colored soil composed of amorphous carbon matter, quartz, feldspar, sulfides, carbonates, various clays, Fe-oxides and hydroxides [94]. It is a common concept in soil science that soil composition and properties is a complex but rather direct function of the mineralogy and geochemistry of rock formations located directly beneath or in the vicinity of the particular soil profile [1,3,12,17,18,22,25]. The principal lithology underlying llicorella soils in the Priorat DOQ region is black shale composed of quartz, feldspar, primary and secondary mica, pyrite, Fe-oxides and hydroxides and carbonates (including siderite FeCO_3 ; Figure 7A). Priorat black shale also contains a number of accessory mineral phases such as sphalerite (Figure 4), xenotime (Figure 6A), (La–Ce–Nd)-monazite (Figure 6B–D), zircon

(Figure 7B,C) and baddeleyite (Figure 7D). However, one of the dominant mineralogical features of these black shale formations is the ubiquitous presence of framboidal Fe-sulfides and oxides (Figure 3). Framboidal mineral structures usually display complex internal microcrystalline microarchitecture formed by globular, octahedral, cubic, truncated-cubic and distorted Fe-rich minerals tightly packed into an external spheroidal form [95–98]. Fe-minerals in framboid structures include predominant pyrite along with magnetite, greigite, limonite and goethite [95,99–102]. Although initially and for a long time framboidal structures were considered to be signs of biogenic activity and biomineralization, other (besides biogenic origin) mechanisms of framboid formation may include (1) specific conditions of microcrystalline nucleation and growth during precipitation from solution; (2) coagulation of magnetic (sulfide, oxide) Fe-rich particles due to magnetic attraction in the presence of strong electrolyte; (3) anoxic diagenesis [95–97,103]. In any case, framboids appear to be sensitive indicators of redox (oxic versus anoxic) conditions during sediment deposition [98,104,105]. We believe that the presence of Fe-minerals (pyrite, magnetite, siderite) and general anoxic (as indicated by framboid developments) environment of volcanic-driven deposition of Priorat black shale will have a lasting effect on the chemical properties of derivative llicorella soil and, consequently, on the properties of grape berries grown on this type of volcanic soil.

Precious metal enrichment is a prominent feature of Priorat black shale. Precious metals occur as native (Figure 5A–C) and cupriferous (Cu = 1.94–4.1 wt.%; Figure 5D–F) silver particles, occasionally hosting micro-inclusions of cuprite (Cu₂O; Figure 5A) and chlorargyrite (AgCl; Figure 5C). Noble metal distribution in bulk black shale samples from the Priorat DOQ region indicate clear enrichments in gold (Au up to 1161 ppb) as well as elevated (0.55–1.58 ppb) platinum concentrations (Table 5). Shoshonitic lava from the Paleozoic black shale/volcaniclastic sequence near Gratallops village also has elevated Pt and Au concentrations (1.24 and 147.32 ppb, respectively; Table 5) and is characterized by clear enrichment of Au over all PGEs (Au/Pt = 118, Au/Ru = 433, Au/Ir = 589, Au/Rh = 1339; Table 5). Comparison of Priorat potassic lava (Figure ??) with shoshonites, primitive basalts and mantle wedge xenoliths from other subduction environments (Papua New Guinea, Fiji, Kamchatka, Tabar-Lihir-Tanga-Feni arc) [106–110] as well as potassic magmas [107] associated with the world-class supergiant Bingham Canyon Cu–Mo–Au deposit in Utah (USA) indicate some general similarities, but also contrasting differences. The distribution of refractory Ir-group PGEs in Priorat shoshonite is broadly similar to other Late Cenozoic arc-related shoshonites as well as Eocene mineralized shoshonite/absarokite stocks at Bingham Canyon (Figure ??). In contrast, the behavior of less-refractory and more mobile (eagerly transported in crustal fluids and hydrothermal solutions [110–115]) Pd-group PGEs and Au in potassic volcanic rocks from the Priorat DOQ region show dramatic differences, such as pronounced negative Pd anomaly (palladium depletion) and Au enrichment, with other shoshonitic magma suites (Figure ??). Gold and, to a lesser extent, palladium and platinum are highly mobile in the presence of chlorine-bearing saline fluids and brines, which may be reflected in the noble metal pattern observed in Priorat shoshonite. Similar geochemical effects have been previously described in explosive rocks from the Lesser Khingan Range in far eastern Russia, where fluids contributed to distribution of Au, Cu and Ag particles during emplacement of volcanic rocks at upper crustal levels [116,117]. This is also consistent with derivation of primary melt for evolved potassic rocks in the Priorat DOQ region from a subduction-related mantle source metasomatically enriched in LILE and noble metals. In addition, involvement of Cl-bearing fluids during Priorat shoshonite genesis and emplacement is consistent with the presence of chlorargyrite (AgCl) micro-inclusions in native silver particles from the black shale accompanying shoshonite magmatism in the Priorat DOQ region (Figure 5C). Enrichment of the volcanic-derived black shale (principal source of the famous llicorella soil) in some platinum-group metals (especially, Pt), Au, Cu (presence of tenorite and cuprite) and Zn (abundant sphalerite) may influence several important processes associated with grape growth, namely (1) rates and specific types of chemical (e.g., alcoholic fermentation, etc.) reactions; (2) levels of

plant metabolites; (3) vine stress response to micronutrient components and (4) expression of specific genes that are involved in the production of compounds that determine (or at least can influence) the aroma and gustatory characteristics of grape and wine [1–27]. Besides the unique geology and high-K geochemistry of the llicorrella soil, the Priorat DOQ region is associated with unusually hot local climate and relatively rugged topography, which helps to mitigate the effects of the daily summer heat [118]. Summers in Priorat are fairly long, dry and hot, with maximum temperatures approaching 35 °C, while winters are quite cold, with minimum temperatures of around −4 °C [118]. Prolonged periods of either freeze or drought are uncommon, as potential incursions of cold air masses from the north are shielded by the carbonate Montsant Cordillera and warm Mistral influence from the Mediterranean coast [118]. With an average annual temperature of 15 °C and annual rainfall of 400–600 mm, coupled with stony llicorella soil low in nitrogen, nutrients and water, winegrowers of Priorat do have a fair share of climatic challenges on their hands. Local topography is very important for wine growing in the region, as rugged relief can be successfully used to offset the extremities of the harsh continental microclimate. The northeastern exposure of many vineyards in Priorat results in the afternoon shade protection of the vines, which, together with the elevated vineyard topography (up to 900 m) and proximity to the sea, effectively assures survival of diurnal variations of about 20 °C, while maintaining the natural acidity and distinctive mineral balance in the Grenache and Carignan grapes that define the classic Priorat red wine blends. Grenache (40%) and Carignan (28%) are the most important vineyard plantings in the Priorat DOQ region, followed by Cabernet Sauvignon (14%), Syrah (12%) and Merlot (6%) [119]. Chemical and physical characteristics of the llicorella soil and its source rocks (mica-rich black shale, high-K volcanics and volcanoclastic sediments) result in low-yield vines directly contributing to the exceptionally high quality of Priorat wines. Similar complex interplays between tectonic, sedimentary, environmental and pedological processes were reported for the coastal volcanic environments of the central and southeastern Tyrrhenian Sea region, contributing to the formation of the unique volcanic terroirs of Latium, Campania, Sicily and Pantelleria [120,121]. Besides specific soil types, elevated and steep topography and diverse and occasionally extreme microclimates, these volcanic terroirs represent special environments of vine growth with clearly decipherable tectonic, mineralogical and geochemical processes and coherent associations of chemical elements (especially noble metals) in soil and underlying volcanic and volcano-derived sedimentary rocks. One of the most interesting and exciting—both in the eyes of geochemists and sophisticated wine connoisseurs—wine terroirs must be volcanic tectonic settings [28–32], of which the famous Priorat DOQ region in Catalonia is, in our humble but firm opinion, an almost perfect example.

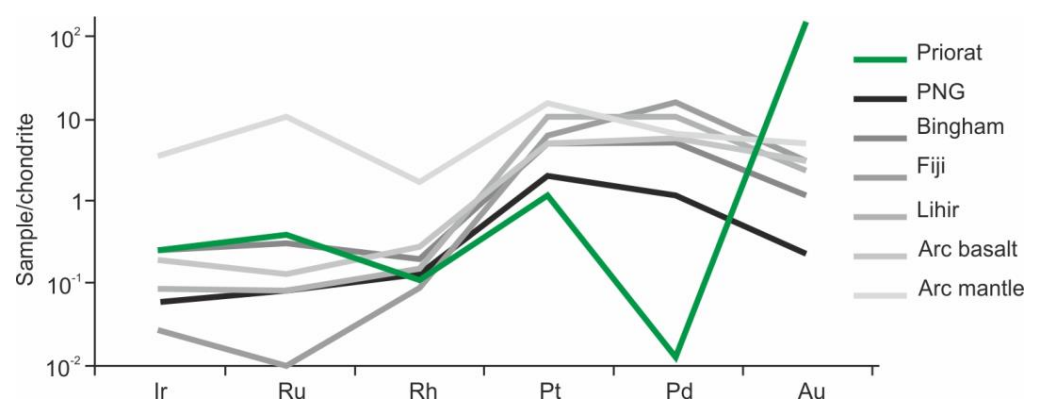


Figure 11. Distribution of platinum-group elements and gold in subduction-related shoshonites, island-arc basalt and island-arc mantle. PNG—Mid-Pleistocene shoshonite lava (average of 32 analyses) from

the Mount Hagen volcano, Papua New Guinea [106]; Bingham—potassic lava associated with giant (>500 million tons of ore), high-grade (>1% Cu and >1 g/t Au) Bingham Canyon Cu–Mo–Au deposit, Utah, USA [107]; Fiji—Late Miocene—Early Pliocene shoshonite associated with high-grade (7 g/t Au) Emperor (Vatukoula) epithermal gold deposit (3.6 Moz of contained Au) in Fiji [107]; Lihir—Late Pleistocene (0.36 Ma) shoshonite associated with giant (56 Moz at 2.3 g/t Au) Ladolam low-sulfidation epithermal gold deposit on the Lihir Island in the Tabar-Lihir-Tanga-Feni island arc near Papua New Guinea [107]; Arc basalt—modern primitive (~9 wt.% MgO) calc-alkaline basalt (average of 12 analyses) from the active Tolbachik volcano, Kamchatka arc [108]; Arc mantle—average (16 analyses) composition of depleted mantle wedge-derived peridotite xenoliths from the Avachinsky volcano, Kamchatka volcanic arc [109,110]. Chondrite normalization values are from [44].

6. Conclusions

The Catalan Coastal Ranges (CCR) in NE Spain is a horst and graben mountain system, which includes deformed (folded and faulted) Paleozoic basement composed in the Priorat DOQ region of Catalonia of black shale, volcanoclastic sediments (sandstone, mudstone, siltstone), potassic lava flows and sills and lithocrystalloclastic tuffs. Both volcanic and volcano-sedimentary rocks are classified as high-K (black shale, volcanoclastic sediments and pyroclastics) and shoshonitic (lava flows and sills) associations, on the basis of K_2O – Na_2O – SiO_2 relationships. Major and trace element variations in detrital sediments indicate their general immaturity, derivation from andesitic to rhyolitic sources and accumulation within an Andean-type active continental margin environment.

Geochemical systematics in volcanic shoshonites show their general trace element-enriched compositional character and suggest derivation from a metasomatized (by recycled sediment melt, adakitic slab melt or slab fluid) variably depleted mantle source in a mature (well-developed), rifted subduction zone setting. We propose that volcano-sedimentary rocks comprising the structural basement of the CCR were formed within the rifted Andean-type margin or Western Pacific-type arc—backarc tectonic environment before being involved in very active Mesozoic–Cenozoic transpressional tectonics along the northeastern margin of the Iberian Massif.

Our new mineralogical and geochemical data suggest that Priorat wine terroir was initially developed in a volcanic-style tectonic setting. Enrichment of black shale, the principal source of world-famous llicorella soil in the Priorat DOQ area, in noble (Pt, Au and Ag) and base (Cu and Zn) metals may have influenced the aromatic and gustatory characteristics of Priorat grapes (“the eight grapes of Priorat”—Grenache, Carignan, Cabernet Sauvignon, Syrah, Merlot, Grenache Blanc, Macabeo and Pedro Ximénez) and, consequently, of internationally celebrated and renowned Priorat wines. Chemical composition of the llicorella soil and its underlying potassic volcanic-sedimentary rocks associated with its nitrogen- and water-poor nature and ability to retain heat (due to the physical properties of such minerals as mica, Fe-oxides and sulfides) account for generally low yields in most Priorat vineyards, resulting in high quality and concentrated flavors of Priorat wines. The nitrogen- and water-depleted stony volcanic-derived soils of Priorat, combined with substantial vineyard elevations, northern exposures and hot microclimate, result in the creation of a unique volcanic terroir, which along with similar geologic environments around the Mediterranean, such as Etna Denominazione di Origine Controllata (DOC) appellation in Sicily, Pantelleria DOC and volcanic DOCs in Campania (Roccamonfina and Vesuvius) and Aglianico del Vulture DOC in Basilicata, provides the world with some of the best examples of perfectly balanced wines with well-structured acidity, elegant minerality and exceptional aromatic characteristics.

Author Contributions: Conceptualization, P.K. and N.K. (Nikita Kepezhinskas); methodology, P.K., N.B. and N.K. (Nikita Kepezhinskas); formal analysis, P.K., N.B., N.K. (Nikita Kepezhinskas), N.K. (Natalia Konovalova), V.K. and I.A.; investigation, P.K., N.B., N.K. (Nikita Kepezhinskas), N.K. (Natalia Konovalova), V.K. and I.A.; resources, P.K., N.B., N.K. (Natalia Konovalova), V.K. and I.A.; data curation, P.K. and N.B.; writing—original draft preparation, P.K.; writing—review and editing, P.K., N.B., N.K. (Nikita Kepezhinskas) and I.A.; visualization, N.B.; supervision, P.K. and N.B.; project administration, P.K., N.B. and N.K. (Nikita Kepezhinskas); funding acquisition, P.K. and N.B.; SEM-EDA, N.K. (Natalia Konovalova); ICP-MS, V.K.; XRF, I.A. All authors have read and agreed to the published version of the manuscript.

Funding: This research received no external funding.

Data Availability Statement: Data are available upon request from the senior author.

Acknowledgments: We thank Luana Moreira Florisbal and an anonymous reviewer for their constructive and helpful reviews of this manuscript. The senior author thanks Irina Kepezhinskas for her assistance during field work in the Priorat region in 2017. P.K. and N.K. express sincere thanks to the owners and staff at the Clos Figueras Winery in Gratallops, Catalonia, Spain, for providing us with comfortable lodging, superb Catalan food and unforgettable wine during our fieldwork in the region in 2019.

Conflicts of Interest: The authors declare no conflict of interest.

References

- Seguin, G. 'Terroirs' and pedology of vinegrowing. *Experientia* **1986**, *42*, 861–873. [[CrossRef](#)]
- Pomerol, C. *The Wines and Winelands of France: Geological Journeys*; Robertson McCarta: London, UK, 1989; 370p.
- Wilson, J.A. *Terroir: The Role of Geology, Climate, and Culture in the Making of French Wines*; University of California Press: Berkeley, CA, USA; Los Angeles, CA, USA, 1998; 336p.
- Hancock, J.M. Feature review—"Terroir; The role of Geology, Climate, and Culture in the making of French Wines". *J. Wine Res.* **1999**, *10*, 43–49. [[CrossRef](#)]
- Huggett, J.M. Geology and wine. *Proc. Geol. Assoc.* **2005**, *117*, 239–247. [[CrossRef](#)]
- Berry, E. *The Wines of Alsace*; The Bodley Head: London, UK, 1993.
- Meinert, L.D.; Busacca, A.J. Terroirs of the Walla Walla Valley appellation, southeastern Washington State, USA. *Geosci. Can.* **2000**, *27*, 149–171.
- Bargmann, C.J. Geology and wine 7: Geology and wine production in the Coastal Region, Western Cape Province, South Africa. *Geosci. Can.* **2003**, *30*, 161–182.
- Cita, M.B.; Chiesa, S.; Colacicchi, R.; Crisci, G.M.; Massiotta, P.; Parotto, M. *Italian Wines and Geology*; BE-MA Editrice: Milano, Italy, 2004; 148p.
- Haynes, S.J. Geology and wine 1: Concept of terroir and the role of geology. *Geosci. Can.* **1999**, *26*, 190–194.
- Tomasi, D.; Gaiotti, F.; Jones, G.V. *The Power of the Terroir: The Case Study of Prosecco Wine*; Springer: Basel, Switzerland, 2013.
- White, R.E. *Soils for the Wines*; Oxford University Press: Oxford, UK, 2003.
- Van Leeuwen, C.; Seguin, G. The concept of terroir in viticulture. *J. Wine Res.* **2006**, *17*, 1–10. [[CrossRef](#)]
- Bourrouilh, R. Geology and terroirs of the Bordeaux wines, France. *Boll. Soc. Geol. Ital. Suppl.* **2006**, *6*, 63–74.
- Maltman, A. The role of vineyard geology in wine typicity. *J. Wine Res.* **2008**, *19*, 1–17. [[CrossRef](#)]
- Pogue, K.R. Folds, floods, and fine wine: Geologic influence on the terroir of the Columbia Basin. In *Volcanoes to Vineyards: Geologic Field Trips through the Dynamic Landscape of the Pacific Northwest*; O'Connor, J.E., Dorsey, R.J., Madin, I.P., Eds.; Geological Society of America Field Guide: Reston, VA, USA, 2009; Volume 15, pp. 1–17.
- Costantini, E.A.C.; Bucelli, P.; Priori, S. Quaternary landscape history determines the soil functional characters of terroir. *Quat. Int.* **2012**, *265*, 63–73. [[CrossRef](#)]
- Imre, S.P.; Kilmartin, P.A.; Rutan, T.; Mauk, J.L.; Nicolau, L. Influence of soil geochemistry on the chemical and aroma profiles of Pinot Noir wines. *J. Food Agric. Environ.* **2012**, *10*, 280–288.
- Angelova, V.R.; Angel, S.I.; Dimitar, M.B. Heavy metals (Pb, Cu, Zn and Cd) in the system soil-grapevine-grape. *J. Sci. Food Agric.* **1999**, *79*, 713–721. [[CrossRef](#)]
- Coetzee, P.P.; Stefens, F.E.; Eiselen, R.J.; Augustyn, O.P.; Balcaens, L.; Vanhaecke, F. Multi-element analysis of South African wines by ICP-MS and their classification according to geographical origin. *J. Agric. Food Chem.* **2005**, *53*, 5060–5066. [[CrossRef](#)]
- Greenough, J.D.; Mallory-Greenough, L.M.; Fryer, B.J. Geology and wine 9: Regional trace element fingerprinting of Canadian wines. *Geosci. Can.* **2005**, *32*, 129–137.
- Kabata-Pendias, A. *Trace Elements in Soils and Plants*, 4th ed.; CRC Press, Taylor & Francis Group: Boca Raton, FL, USA, 2011; 432p.
- Protano, G.; Rossi, S. Relationship between soil geochemistry and grape composition in Tuscany (Italy). *J. Plant Nutr. Soil Sci.* **2014**, *177*, 500–508. [[CrossRef](#)]

24. Pepi, S.; Sansone, L.; Chicca, M.; Vaccaro, C. Relationship among geochemical elements in soil and grapes as terroir fingerprintings in *Vitis vinifera* L. cv. “Glera”. *Chem. Erde* **2017**, *77*, 121–130. [[CrossRef](#)]
25. Retallack, G.J.; Burns, S.F. The effects of soil on the taste of wine. *GSA Today* **2016**, *26*, 4–9. [[CrossRef](#)]
26. Young, Y.; Duan, C.; Du, H.; Tian, J.; Pan, Q. Trace element and rare earth element profiles in berry tissues of three grape cultivars. *Am. J. Enol. Vitic.* **2010**, *61*, 401–407. [[CrossRef](#)]
27. Censi, P.; Saiano, F.; Pisciotta, A.; Tuzzolino, N. Geochemical behavior in rare earths in *Vitis vinifera* grafted onto different rootstocks and growing on several soils. *Sci. Total Environ.* **2014**, *473–474*, 597–608. [[CrossRef](#)]
28. Szabo, J. *Volcanic wines: Salt, Grit and Power*; Jacqui Small: London, UK, 2016; 256p.
29. Frankel, C. *Volcanoes and Wine: From Pompei to Napa*; University of Chicago Press: Chicago, IL, USA, 2019; 216p.
30. Kepezhinskas, P. *Geologic History of Wine*; Knig-Izdat: Moscow, Russia, 2021; 261p. (In Russian)
31. Kepezhinskas, P. *Hephaestus and Dionysus: Volcanic Wine Terroirs*; Knig-Izdat: Moscow, Russia, 2022; 249p. (In Russian)
32. Swinchatt, J.P.; Howell, D.G.; MacDonald, S.L. The scale dependence of wine and terroir: Examples from coastal California and the Napa Valley (USA). *Elements* **2018**, *14*, 179–184. [[CrossRef](#)]
33. Thomaidis, K.; Troll, V.R.; Deegan, F.M.; Freda, C.; Corsaro, R.A.; Behncke, B.; Rafailidis, S. A message from the ‘underground forge of the gods’: History and current eruptions at Mt Etna. *Geol. Today* **2021**, *37*, 141–149. [[CrossRef](#)]
34. Diaz-Acha, Y.; Campeny, M.; Casas, L.; Di Febo, R.; Ibañez-Insa, J.; Jawhari, T.; Bosch, J.; Borrell, F.; Jorge-Villar, S.E.; Greneche, J.-M.; et al. Colours of gemmy phosphates from the Gavà Neolithic mines (Catalonia, Spain): Origin and archaeological significance. *Minerals* **2022**, *12*, 368. [[CrossRef](#)]
35. Izquierdo-Llavall, E.; Ayala, C.; Pueyo, E.L.; Casas-Sainz, A.M.; Oliva-Urcia, B.; Rubio, F.; Rodriguez-Pintó, A.; Rey-Moral, C.; Mediato, J.F.; Garcia-Crespo, J. Basement-cover relationships and their along-strike changes in the linking zone (Iberian Range, Spain): A combined structural and gravimetric study. *Tectonics* **2019**, *38*, 2934–2960. [[CrossRef](#)]
36. Juez-Larré, J.; Andriessen, P.A.M. Post Late Paleozoic tectonism in the southern Catalan Coastal Ranges (NE Spain), assessed by apatite fission track analysis. *Tectonophysics* **2002**, *349*, 113–129. [[CrossRef](#)]
37. Gaspar-Escribano, J.M.; Roca, E.; Cloetingh, S. Cenozoic vertical motions of the Catalan Coastal Ranges. *Tectonics* **2004**, *23*, TC1004. [[CrossRef](#)]
38. Marin, M.; Roca, E.; Marcuello, A.; Cabrera, L.; Ferrer, O. Mesozoic structural inheritance in the Cenozoic evolution of the central Catalan Coastal Ranges (western Mediterranean): Structural and magnetotelluric analysis in the Gaià-Montmell High. *Tectonophysics* **2021**, *814*, 228970. [[CrossRef](#)]
39. Berdnikov, N.; Kepezhinskas, P.; Konovalova, N.; Kepezhinskas, N. Formation of gold alloys during crustal differentiation of convergent zone magmas: Constraints from Au-rich websterite in the Stanovoy Suture Zone (Russian Far East). *Geosciences* **2022**, *12*, 126. [[CrossRef](#)]
40. Jin, X.; Zhu, H. Determination of platinum-group elements and gold in geological samples with ICP-MS using sodium peroxide fusion and tellurium co-precipitation. *J. Anal. At. Spectrom.* **2000**, *15*, 747–751. [[CrossRef](#)]
41. Kepezhinskas, P.; Berdnikov, N.; Konovalova, N.; Kepezhinskas, N.; Krutikova, V.; Kirichenko, E. Native metals and alloys in trachytes and shoshonite from the continental United States and high-K dacite from the Bolivian Andes: Magmatic origins of ore metals in convergent and within-plate tectonic settings. *Russ. J. Pac. Geol.* **2022**, *16*, 405–426. [[CrossRef](#)]
42. Whitney, D.L.; Evans, B.W. Abbreviations for names of rock-forming minerals. *Am. Mineral.* **2010**, *95*, 185–187. [[CrossRef](#)]
43. Sun, S.S.; McDonough, W.F. Chemical and isotopic systematics of oceanic basalts: Implications for mantle composition and processes. *Geol. Soc. Lond. Spec. Publ.* **1989**, *42*, 313–345. [[CrossRef](#)]
44. Taylor, S.R.; McLennan, S.M. *The Continental Crust: Its Composition and Evolution*; Blackwell: Oxford, UK, 1985; 312p.
45. Gest, D.; McBirney, A.R. Genetic relations of shoshonitic and absarokitic magmas, Absaroka Mountains, Wyoming. *J. Volcanol. Geotherm. Res.* **1979**, *6*, 85–104. [[CrossRef](#)]
46. Morrison, G. Characteristics and tectonic setting of the shoshonite rock association. *Lithos* **1980**, *13*, 97–108. [[CrossRef](#)]
47. Hole, M.J.; Saunders, A.D.; Marriner, G.F.; Tarney, J. Subduction of pelagic sediments: Implications for the origin of Ce-anomalous basalts from the Mariana Islands. *J. Geol. Soc.* **1984**, *141*, 453–472. [[CrossRef](#)]
48. Neal, C.R.; Taylor, L.A. A negative Ce anomaly in a peridotite xenolith: Evidence for crustal recycling into the mantle or mantle metasomatism? *Geochim. Cosmochim. Acta* **1989**, *53*, 1035–1040. [[CrossRef](#)]
49. Ben Othman, D.; White, W.M.; Patchett, J. The geochemistry of marine sediments, island arc magma genesis, and crust-mantle recycling. *Earth Planet. Sci. Lett.* **1989**, *94*, 1–21. [[CrossRef](#)]
50. Zhang, M.; Yu, Y.; Choi, J.; Cai, K.; Shi, M. Petrography and geochemistry of clastic sedimentary rocks as evidence for the provenance of the Jurassic stratum in the Daqingshan area. *Open Geosci.* **2020**, *12*, 1350–1368. [[CrossRef](#)]
51. Bhatia, M.R.; Crook, K.A.W. Trace element characteristics of graywackes and tectonic setting discrimination of sedimentary basins. *Contrib. Mineral. Petrol.* **1986**, *92*, 181–193. [[CrossRef](#)]
52. Maynard, J.B.; Valloni, R.; Yu, H.S. Composition of modern deep-sea sands from arc-related basins. *Geol. Soc. Lond. Spec. Publ.* **1982**, *10*, 551–561. [[CrossRef](#)]
53. Gu, X.X.; Liu, J.M.; Zheng, M.H.; Tang, J.X.; Qi, L. Provenance and tectonic setting of the Proterozoic turbidites in Hunan, south China: Geochemical evidence. *J. Sediment Res.* **2002**, *72*, 393–407. [[CrossRef](#)]
54. Floyd, P.A.; Leveridge, B.E. Tectonic environment of the Devonian Gramscatho basin, South Cornwall: Framework mode and geochemical evidence from turbidite sandstones. *J. Geol. Soc. Lond.* **1987**, *144*, 531–542. [[CrossRef](#)]

55. Floyd, P.A.; Winchester, J.A.; Park, R.G. Geochemistry and tectonic setting of Lewisian clastic metasediments from the Early Proterozoic Loch Maree group of Gairloch, NW Scotland. *Precambrian Res.* **1989**, *45*, 203–214. [[CrossRef](#)]
56. Peccerillo, A.; Taylor, S.R. Geochemistry of Eocene calc-alkaline volcanic rocks from the Kastamonu area, Northern Turkey. *Contrib. Mineral. Petrol.* **1976**, *58*, 63–81. [[CrossRef](#)]
57. Pe-Piper, G.; Piper, D.J.W.; Koukouvelas, I.; Dolansky, L.M.; Kokkalas, S. Postorogenic shoshonitic rocks and their origin by melting underplated basalts: The Miocene of Limnos, Greece. *Geol. Soc. Amer. Bull.* **2009**, *121*, 39–54. [[CrossRef](#)]
58. Kepezhinskas, P. Diverse shoshonite magma series in the Kamchatka Arc: Relationships between intra-arc extension and composition of alkaline magmas. *Geol. Soc. Lond. Spec. Publ.* **1994**, *81*, 249–264. [[CrossRef](#)]
59. Pearce, J.A. Geochemical fingerprinting of oceanic basalts with applications to ophiolite classification and the search for Archean oceanic crust. *Lithos* **2008**, *100*, 14–48. [[CrossRef](#)]
60. Shervais, J.W. The petrogenesis of modern and ophiolitic lavas reconsidered: Ti-V and Nb-Th. *Geosci. Front.* **2022**, *13*, 101319. [[CrossRef](#)]
61. Condie, K.C. High field strength element ratios in Archean basalts: A window to evolving sources of mantle plumes? *Lithos* **2005**, *79*, 491–504. [[CrossRef](#)]
62. Murphy, J.B.; MacDonald, D.L. Geochemistry and tectonic discrimination of Late Proterozoic arc-related volcanoclastic turbidite sequences, Antigonish Highlands, Nova Scotia. *Can. J. Earth Sci.* **1993**, *30*, 2273–2282. [[CrossRef](#)]
63. Verma, S.P.; Armstrong-Altrin, J.S. Geochemical discrimination of siliciclastic sediments from active and passive margin settings. *Sed. Geol.* **2016**, *332*, 1–12. [[CrossRef](#)]
64. Gill, J.B.; Hiscott, R.N.; Vidal, P. Turbidite geochemistry and evolution of the Izu-Bonin arc and continents. *Lithos* **1994**, *33*, 135–168. [[CrossRef](#)]
65. Briquieu, L.; Bougault, H.; Joron, J.L. Quantification of Nb, Ta, Ti and V anomalies in magmas associated with subduction zones: Petrogenetic implications. *Earth Planet. Sci. Lett.* **1984**, *68*, 297–308.
66. Ryerson, F.J.; Watson, E.B. Rutile saturation in magmas: Implications for Ti-Nb-Ta depletion in island-arc basalts. *Earth Planet. Sci. Lett.* **1987**, *86*, 225–239. [[CrossRef](#)]
67. Schmidt, M.W.; Jagoutz, O. The global systematics of primitive arc melts. *Geochem. Geophys. Geosyst.* **2017**, *18*, 2817–2854. [[CrossRef](#)]
68. Cousens, B.L.; Allan, J.F.; Gorton, M.P. Subduction-modified pelagic sediments as the enriched component in back-arc basalts from the Japan Sea: Ocean Drilling Program Sites 797 and 794. *Contrib. Mineral. Petrol.* **1994**, *117*, 421–434. [[CrossRef](#)]
69. Gamble, J.; Woodhead, J.; Wright, I.; Smith, I. Basalt and sediment geochemistry and magma petrogenesis in a transect from oceanic island arc to rifted continental margin arc: The Kermadec-Hikurangi margin, SW Pacific. *J. Petrol.* **1996**, *37*, 1525–1546. [[CrossRef](#)]
70. Karig, D.E.; Moore, G.F. Tectonically controlled sedimentation in marginal basins. *Earth Planet. Sci. Lett.* **1975**, *26*, 233–238.
71. Underwood, M.B.; Balance, P.F.; Clift, P.D.; Hiscott, R.N.; Marsaglia, K.M.; Pickering, K.T.; Reid, R.P. Sedimentation in forearc basins, trenches, and collision zones of the Western Pacific: A summary of results from the Ocean Drilling Program. *Geophys. Monogr. Ser.* **1995**, *88*, 315–353.
72. Clift, P.D.; ODP Leg 135 Scientific Party. Volcanism and sedimentation in a rifting island-arc terrain: An example from Tonga, SW Pacific. *Geol. Soc. Lond. Spec. Publ.* **1994**, *81*, 29–51.
73. Pe-Piper, G.; Piper, D.J.W. Spatial and temporal variation in Late Cenozoic back-arc volcanic rocks, Aegean Sea region. *Tectonophysics* **1989**, *169*, 113–134. [[CrossRef](#)]
74. Perkins, R.J.; Cooper, F.J.; Condon, D.J.; Ttattitch, B.; Naden, J. Post-collisional Cenozoic extension in the northern Aegean: Three high-K to shoshonitic intrusive rocks of the Maronia Magmatic Corridor, northeastern Greece. *Lithosphere* **2018**, *10*, 582–601. [[CrossRef](#)]
75. Campbell, I.H.; Stepanov, A.S.; Liang, H.-Y.; Allen, C.M.; Norman, M.D.; Zhang, Y.-Q.; Xie, Y.-W. The origin of shoshonites: New insights from the tertiary high-potassium intrusions of eastern Tibet. *Contrib. Mineral. Petrol.* **2014**, *167*, 983. [[CrossRef](#)]
76. Yücel, C.; Arslan, M.; Temizel, I.; Yazar, E.A.; Ruffet, G. Evolution of K-rich magmas derived from a next veined lithospheric mantle in an ongoing extensional setting: Geochronology and geochemistry of Eocene and Miocene volcanic rocks from Eastern Pontides (Turkey). *Gondwana Res.* **2017**, *45*, 65–86. [[CrossRef](#)]
77. Callegari, E.; Cigolini, C.; Medeot, O.; D'Antonio, M. Petrogenesis of calc-alkaline and shoshonitic post-collisional Oligocene volcanics of the Cover Series of the Sezia Zone, Western Italian Alps. *Geodin. Acta* **2004**, *17*, 1–29. [[CrossRef](#)]
78. Conticelli, S.; Guarnieri, L.; Farinelli, A.; Mattei, M.; Avanzinelli, R.; Bianchini, G.; Boari, E.; Tommasini, S.; Tiepolo, M.; Prelevic, D.; et al. Trace elements and Sr-Nd-Pb isotopes of K-rich, shoshonitic, and calc-alkaline magmatism of the Western Mediterranean Region: Genesis of ultrapotassic to calc-alkaline magmatic associations in a post-collisional geodynamic setting. *Lithos* **2009**, *107*, 68–92. [[CrossRef](#)]
79. Aitchison, J.C.; McDerimid, I.R.C.; Ali, J.R.; Davis, A.M.; Zyabrev, S.V. Shoshonites in Southern Tibet record Late Jurassic rifting of a Tethyan intraoceanic island arc. *J. Geol.* **2007**, *115*, 197–213. [[CrossRef](#)]
80. Kent, A.J.R.; Elliott, T.R. Melt inclusions from Marianas arc lavas: Implications for the composition and formation of island arc magmas. *Chem. Geol.* **2002**, *183*, 263–286. [[CrossRef](#)]
81. Hochstaedter, A.G.; Kepezhinskas, P.; Defant, M.J.; Drummond, M.S.; Koloskov, A. Insights into the volcanic arc mantle wedge from magnesian lavas from the Kamchatka arc. *J. Geophys. Res.* **1996**, *101*, 697–712. [[CrossRef](#)]

82. Einsele, G. Basaltic sill-sediment complexes in young spreading centers: Genesis and significance. *Geology* **1985**, *13*, 249–252. [[CrossRef](#)]
83. Bell, B.; Butcher, H. On the emplacement of sill complexes: Evidence from the Faroe-Shetland Basin. *Geol. Soc. Lond. Spec. Publ.* **2002**, *197*, 307–329. [[CrossRef](#)]
84. Jourdain, A.; Singh, S.C.; Escartin, J.; Klinger, Y.; Kamesh Raju, K.A.; McArdle, J. Crustal accretion at a sedimented spreading center in the Andaman Sea. *Geology* **2016**, *44*, 351–354. [[CrossRef](#)]
85. Kepezhinskas, V.V. Calc-alkaline sheeted dikes in ophiolite complexes as indicators of intra-arc spreading. *Rep. USSR Acad. Sci.* **1984**, *278*, 700–703. (In Russian)
86. Leitch, E.C. Island arc elements and arc-related ophiolites. *Tectonophysics* **1984**, *106*, 177–203. [[CrossRef](#)]
87. Julivert, M.; Duran, H. The Hercynian structure of the Catalanian Coastal Ranges (NE Spain). *Acta Geol. Hisp.* **1990**, *25*, 13–21.
88. Julivert, M.; Duran, H. Paleozoic stratigraphy of the Central and Northern part of the Catalanian Coastal Ranges (NE Spain). *Acta Geol. Hisp.* **1990**, *25*, 3–12.
89. Kepezhinskas, N.; Kamenov, G.D.; Foster, D.A.; Kepezhinskas, P. Petrology and geochemistry of alkaline basalts and gabbroic xenoliths from Utila Island (Bay Islands, Honduras): Insights into back-arc processes in the Central American Volcanic Arc. *Lithos* **2020**, *352–353*, 105306. [[CrossRef](#)]
90. Kepezhinskas, P.; Berdnikov, N.; Kepezhinskas, N.; Konovalova, N. Adakites, high-Nb basalts and copper-gold deposits in magmatic arcs and collisional orogens: An overview. *Geosciences* **2022**, *12*, 29. [[CrossRef](#)]
91. Kepezhinskas, P.; Defant, M.J.; Drummond, M.S. Progressive enrichment of island arc mantle by melt-peridotite interaction inferred from Kamchatka xenoliths. *Geochim. Cosmochim. Acta* **1996**, *60*, 1217–1229. [[CrossRef](#)]
92. Drummond, M.S.; Defant, M.J.; Kepezhinskas, P.K. Petrogenesis of slab-derived trondhjemite-tonalite-dacite/adakite magmas. *Earth Environ. Sci. Trans. R. Soc. Edinb.* **1996**, *87*, 205–215.
93. Defant, M.J.; Kepezhinskas, P. Evidence suggests slab melting in arc magma. *EOS Trans. Amer. Geophys. Union* **2001**, *82*, 65–69. [[CrossRef](#)]
94. Maltman, A. Minerality in wine: A geological perspective. *J. Wine Res.* **2013**, *24*, 169–181. [[CrossRef](#)]
95. Rickard, D.T. The origin of framboids. *Lithos* **1970**, *3*, 269–293.
96. Sawlowicz, Z. Pyrite framboids and their development: A new conceptual mechanism. *Geologische Rundschau* **1993**, *82*, 148–156.
97. Ohfuji, H.; Rickard, D. Experimental synthesis of framboids—A review. *Earth-Sci. Rev.* **2005**, *71*, 147–170.
98. Gallego-Torres, D.; Reolid, M.; Nieto-Moreno, V.; Martine-Casado, F.J. Pyrite framboid size distribution as a record for relative variations in sedimentation rate: An example on the Toarcian Oceanic Anoxic Event in South Iberian paleomargin. *Sed. Geol.* **2015**, *330*, 59–73. [[CrossRef](#)]
99. Loughheed, M.S.; Mancuso, J.J. Hematite framboids in the Negaunee Iron Formation, Michigan: Evidence for their biogenic origin. *Econ. Geol.* **1973**, *68*, 202–209. [[CrossRef](#)]
100. Ahn, J.H.; Buseck, P.R. Hematite nanospheres of possible colloidal origin from a Precambrian banded iron formation. *Science* **1990**, *250*, 111–113. [[CrossRef](#)] [[PubMed](#)]
101. Suk, D.; Peacor, D.R.; Van der Voo, R. Replacement of pyrite framboids by magnetite in limestone and implications for paleomagnetism. *Nature* **1990**, *345*, 611–613. [[CrossRef](#)]
102. Kalatha, S.; Economou-Eliopoulos, M. Framboidal pyrite and bacteriomorphic goethite at transitional zones between Fe-Ni-laterites and limestones: Evidence from Lokris, Greece. *Ore Geol. Rev.* **2015**, *65*, 413–425.
103. Wilkin, R.T.; Barnes, H.L. Formation processes of framboidal pyrite. *Geochim. Cosmochim. Acta* **1997**, *61*, 323–339. [[CrossRef](#)]
104. Raiswell, R.; Berner, R.A. Pyrite formation in euxinic and semi-euxinic sediments. *Am. J. Sci.* **1985**, *285*, 710–724. [[CrossRef](#)]
105. Wilkin, R.T.; Barnes, H.L.; Brantley, S.L. The size distribution of framboidal pyrite in modern sediments: An indicator of redox conditions. *Geochim. Cosmochim. Acta* **1996**, *60*, 3897–3912. [[CrossRef](#)]
106. Misztela, M.A.; Campbell, I.H.; Arculus, R.J. Platinum-group element geochemistry and magma evolution of the Mount Hagen (Papua New Guinea) magmatic system. *J. Petrol.* **2022**, *63*, 1–20. [[CrossRef](#)]
107. Maughan, D.; Keith, J.D.; Christiansen, E.H.; Pulsipher, T.; Hattori, K.; Evans, N.J. Contributions from mafic alkaline magmas to the Bingham porphyry Cu-Au-Mo deposit, Utah, USA. *Mineral. Depos.* **2002**, *37*, 14–37. [[CrossRef](#)]
108. Kuttyrev, A.; Zelenski, M.; Nekrylov, N.; Savelyev, D.; Kontonikas-Charos, A.; Kamenetsky, V.S. Noble metals in arc basaltic magmas worldwide: A case study of modern and pre-historic lavas of the Tolbachik volcano, Kamchatka. *Front. Earth Sci.* **2021**, *9*, 1199. [[CrossRef](#)]
109. Kepezhinskas, P.; Defant, M.J.; Widom, E. Abundance and distribution of PGE and Au in the island-arc mantle: Implications for sub-arc metasomatism. *Lithos* **2002**, *60*, 113–128. [[CrossRef](#)]
110. Widom, E.; Kepezhinskas, P.; Defant, M.J. The nature of metasomatism in the sub-arc mantle wedge: Evidence from Re-Os isotopes in Kamchatka peridotite xenoliths. *Chem. Geol.* **2003**, *196*, 283–306. [[CrossRef](#)]
111. McKibben, M.A.; Williams, A.E.; Hall, G.E.M. Solubility and transport of platinum-group elements and Au in saline hydrothermal fluids: Constraints from geothermal brine data. *Econ. Geol.* **1990**, *85*, 1926–1934. [[CrossRef](#)]
112. Tassara, S.; González-Jiménez, J.M.; Reich, M.; Saunders, E.; Luguét, A.; Morata, D.; Grégoire, M.; van Acken, D.; Schilling, M.E.; Barra, F.; et al. Highly siderophile elements mobility in the subcontinental lithospheric mantle beneath southern Patagonia. *Lithos* **2018**, *314–315*, 579–596. [[CrossRef](#)]

113. Tagirov, B.R.; Filimonova, O.; Trigub, A.L.; Akinfiyev, N.N.; Nickolsky, M.S.; Kvashnina, K.O.; Chareev, D.A.; Zotov, A.V. Platinum transport in chloride-bearing fluids and melts: Insights from in situ X-ray absorption spectrometry and thermodynamic modeling. *Geochim. Cosmochim. Acta* **2019**, *254*, 86–101. [[CrossRef](#)]
114. Wood, S.A.; Normand, C. Mobility of palladium chloride complexes in mafic rocks: Insights from a flow-through experiment at 25 °C using air-saturated, acidic, and Cl-rich solutions. *Mineral. Petrol.* **2008**, *92*, 81–97. [[CrossRef](#)]
115. Hanley, J.J.; Mungall, J.E.; Pettke, T.; Spooner, E.T.C.; Bray, C.J. Fluid and halide melt inclusions of magmatic origin in the Ultramafic and Lower Banded Series, Stillwater Complex, Montana, USA. *J. Petrol.* **2008**, *49*, 1133–1160. [[CrossRef](#)]
116. Berdnikov, N.; Nevstruev, V.; Kepezhinskas, P.; Astapov, I.; Konovalova, N. Gold in mineralized volcanic systems from the Lesser Khingan Range (Russian Far East): Textural types, composition and possible origins. *Geosciences* **2021**, *11*, 103. [[CrossRef](#)]
117. Berdnikov, N.V.; Nevstruev, V.G.; Kepezhinskas, P.K.; Krutikov, V.O.; Astapov, I.A. Silicate, Fe-oxide, and Au-Cu-Ag microspherules in ores and pyroclastic rocks of the Kostenga iron deposit in the Far East of Russia. *Russ. J. Pac. Geol.* **2021**, *15*, 236–251. [[CrossRef](#)]
118. Barcelona Field Studies Centre. Available online: geographyfieldwork.com/PrioratClimate.html (accessed on 9 January 2023).
119. Wine Folly. Available online: winefolly.com/deep-dive/in-search-of-the-best-wines-from-priorat (accessed on 10 January 2023).
120. Gamberi, F.; Della Valle, G.; Marani, M.; Mercorella, A.; Distefano, S.; Di Stefano, A. Tectonic controls on sedimentary system along the continental slope of the central and southeastern Tyrrhenian Sea. *Ital. J. Geosci.* **2019**, *138*, 317–332. [[CrossRef](#)]
121. Borzi, L.; Anfuso, G.; Manno, G.; Distefano, S.; Urso, S.; Chiarella, D.; Di Stefano, A. Shoreline evolution and environmental changes at the NW area of the Gulf of Gela (Sicily, Italy). *Land* **2021**, *10*, 1034. [[CrossRef](#)]

Disclaimer/Publisher’s Note: The statements, opinions and data contained in all publications are solely those of the individual author(s) and contributor(s) and not of MDPI and/or the editor(s). MDPI and/or the editor(s) disclaim responsibility for any injury to people or property resulting from any ideas, methods, instructions or products referred to in the content.